Received: 27 March 2024 | Accepted: 19 May 2024

DOI: 10.1002/est2.668

RESEARCH ARTICLE

ENERGY STORAGE WILEY

Enhanced energy density of high entropy alloy (Fe-Co-Ni-Cu-Mn) and green graphene hybrid supercapacitor

Gobinda Chandra Mohanty[1] | **Chinmayee Chowde Gowda**[1] | **Pooja Gakhad**[2] | **Anu Verma**[3] | **Shubhasikha Das**[3] | **Shamik Chowdhary**[3] | **Jayanta Bhattacharya**[3,4] | **Abhishek K Singh**[2] | **Koushik Biswas**[1,5] | **Chandra Sekhar Tiwary**[1,5]

[1]School of Nano Science and Technology, Indian Institute of Technology, Kharagpur, West Bengal, India

[2]Materials Research Centre, Indian Institute of Science, Bengaluru, India

[3]School of Environmental Science and Technology, Indian Institute of Technology, Kharagpur, West Bengal, India

[4]Department of Mining Engineering, Indian Institute of Technology, Kharagpur, West Bengal, India

[5]Department of Metallurgical and Materials Engineering, Indian Institute of Technology, Kharagpur, West Bengal, India

Correspondence
Chandra Sekhar Tiwary and and Koushik Biswas, School of Nano Science and Technology, Indian Institute of Technology, Kharagpur, West Bengal, 721302, India.
Email: chandra.tiwary@metal.iitkgp.ac.in and k_biswas@metal.iitkgp.ac.in

Abhishek K Singh, Materials Research Centre, Indian Institute of Science, Bengaluru, 560012, India.
Email: abhishek@iisc.ac.in

Funding information
Core research grant of SERB-India, STARS project by MHRD-India, DAE Young Scientist Research Award (DAEYSRA); AOARD (Asian Office of Aerospace Research and Development), Grant/Award Number: FA2386-23-14034; Naval research board (NRB)

Abstract

Given the growing demand for new materials for supercapacitor applications, high entropy alloys (HEAs) are being extensively investigated. They are an efficient alternative to existing energy sources due to their synergistic contribution from individual element. We demonstrate the development of nanostructured HEA (FeCoNiCuMn) as a cathode material with specific capacitance (C_s) of ~388 F g^{-1} (5 mV s^{-1}). As anode material, green graphene (rice straw biochar) synthesized using pyrolysis shows a maximum C_s of ~560 F g^{-1} at similar scan rate (5 mV s^{-1}). A hybrid asymmetric liquid state device was assembled using the FeCoNiCuMn nanostructured HEA and green graphene as electrodes. Utilizing the green source, the device provided a high C_s of 83.22 F g^{-1} at 2 A g^{-1}. The specific energy of the device was 33.4 Wh kg^{-1} and specific power of 1.7 kW kg^{-1}. The electrochemical behavior of each element in the high entropy composition was studied through post X-ray photoelectron spectroscopy and scanning electron microscopic analysis. The chemical behavior of FeCoNiCuMn is further investigated using DFT studies. The enhanced electrochemical properties and synergistic contribution of each element of the HEA is studied via *d*-band theory. The current study can be utilized to develop asymmetric hybrid supercapacitors as environmental friendly energy source.

Gobinda Chandra Mohanty, Chinmayee Chowde Gowda, and Pooja Gakhad have contributed equally to this study.

KEYWORDS

DFT analysis, FeCoNiCuMn, green graphene, high entropy alloy, supercapacitor, XPS studies

1 | INTRODUCTION

Supercapacitors have gained more research attention because of their high energy density, long-term cyclic stability, also for its bridging functionality between traditional capacitors and batteries.[1,2] In this aspect, various electrode materials are developed for supercapacitors; metal oxides,[3] chalcogenides,[4] metal carbides,[5,6] and porous carbon derivatives[7] are among primary choices. In the strategy of the current energy storage sources such as: Li-ion batteries,[8] aqueous Zn-ion batteries,[9,10] lithium-selenium batteries,[11] aqueous ammonium-ion batteries,[12] Li-S batteries,[13] hybrid-ion batteries[14] and supercapacitors[15] play an important role providing a diverse range of electrode material. The energy storage device's safety and sustainability can be demonstrated in batteries, supercapacitors and other energy devices.[16,17] Similarly, the prediction of the life cycle assessment at various temperature can be done by improved short-term memories,[18] the state of health monitoring can be studied based on electrochemical impedance spectroscopy.[19] Synthesizing of the above materials involve chemical routes and requires tuning or addition of other elements. In order to surpass this issue and also to bypass the concept of doping, researchers have employed high entropy alloy (HEA) based materials for electrochemical applications.[20,21] These HEAs offer an effective way to produce multivalent quinary framework for higher electrochemical activity. The performance in disordered multi metallic system is due to various characteristic effects such as cocktail, lattice distortion and high entropy effects that boosts the electrochemical catalytic activity and charge storage property.[22]

Among various HEA-based supercapacitors, $(FeCoCrMnNi)_3O_4$,[23] $(CrMnFeCoNi)_3O_4$,[24] $(FeCoCrMnZn)_3O_4$,[25] AlCoCrFeNi,[26] and FeNiCoMnMg HEA-NPs/ACNFs[27] along with HEA-based composites, rHEO−CNT,[28] HEO/f-CSAC,[29] NiCuFeCoMn-carbonate,[30] are among a few HEA explored in the field. In addition to high entropy based supercapacitive materials, various phosphate composed of similar compositions of supercapacitive materials like Fe, Co, Mn, and Ni are reported till date. Among them, cobalt manganese phosphate thin film displays highest C_s of 571 F g^{-1} at 2.2 A g^{-1} with nano/micro flower like morphology on stainless steel as substrate.[31] In addition, amorphous Fe-doped nickel-cobalt phosphate ($Fe_xNiCo[PO_4]_2$) thin film shows nanoparticles like morphology displaying highest C_s of 987 C g^{-1} at 2.1 A g^{-1} with excellent cyclic stability 95.3% after 5000 cycles.[32] Amorphous nickel-manganese phosphate on graphene nano hills covered with carbon cloth showed highest capacity of 1068 C g^{-1} at current density of 3 A g^{-1} with 97% capacity retention after 5000 cycles.[33]

Along with the HEA as cathode, biochar derived from agricultural waste was tested as anode for supercapacitor device. The material has grasped attention in areas such as energy storage due to easy synthesis, better chemical sustainability, cost-effectiveness, and high C_s (carbon derivatives). Rice straw is a prominent agricultural waste in India, China, and other South Asian countries. The wide availability of raw materials leads to biochar produced by carbonization and has been used for various applications in areas like corrosion resistance,[34] wastewater treatment,[35] increasing soil fertility, catalysis, gas sensing, energy storage and many more.[36-38] The article presents the production of green graphene (biochar) from rice straw agricultural waste by pyrolysis techniques. The required compositional, morphological characterizations were done along with three electrode measurements.

In this regard, we synthesized low-cost FeCoNiCuMn single-phase alloy via induction melting later crushed them into nanostructures by high energy vibratory ball milling. The required characterizations were done on these powdered samples to understand structural, morphological, and compositional characteristics. These surface oxidized quinary elements (Fe^{2+}, Co^{2+}, Ni^{2+}, Cu^{+}, Mn^{3+}, and Mn^{4+}) significantly show electrochemical activity with aqueous potassium hydroxide (KOH) electrolyte. Further, FeCoNiCuMn HEA and rice straw biochar are used as positive and negative electrode, respectively, for fabricating a liquid state asymmetric device. We perform first principal calculations for the HEA and device performance of the material as a supercapacitor was studied thoroughly. The DFT study was used to study *d*-band center effects. Additionally, when comparing the Mn atom in the FeCoNiCuMn nanocluster to an individual, the OH^- activation energy evaluated with change in adsorption energy is maximum, and Ni has the lowest adsorption energy. Post electrochemical measurements were performed in order to find insights into the material behavior after continuous cycling for longer durations. The post electrochemical studies were thoroughly studied. A comparison of surface and

diffusion controlled process with FeCoNiCuZn/Mn systems as Mn replacement of Zn was analyzed in detail along with first principle calculations involving *d*-band calculations and OH adsorption within various elements.

2 | MATERIALS AND METHODS

2.1 | Preparation FeCoNiCuMn HEA

All metals (Fe, Co, Ni, Cu, and Mn) for synthesizing HEA were purchased from Loba Chemie, India. Acetylene carbon black from Alfa Aesar (CAS No: 1333-86-4), polyvinylidene fluoride (CAS No: 24937-79-9), and potassium hydroxide (CAS No: 1310-58-3) are from Merck India. Solvent N-methyl-2-pyrolidone (NMP) was purchased from Loba Chemie (CAS No: 872-50-4).

Induction melting was used for the synthesis of FeCoNiCuMn HEA. An equimolar (0.2 M) mixture of Fe, Co, Ni, Cu, and Mn is vacuum sealed in a quartz tube. The melting procedure was carried out several times at 1150°C to ensure chemical homogeneity of bulk HEA ingot. The ingot is then placed for heat treatment for 12 h at 1000°C. Single-phase formation was confirmed via XRD and ingot was fragmented and was subsequently ground into powder an agglomerated structure using a high-energy vibratory ball mill. The schematic of the synthesis protocol is shown below in Figure 1.

2.2 | Preparation of Green graphene

Rice straw biochar was synthesized by pyrolysis of rice straw agricultural waste collected from agricultural fields near IIT Kharagpur campus. The collected rice straws were cleaned several times with double-distilled water and completely dehydrated at 70°C for 48 h in a hot air oven. Later heat treated to form small particles of 1 to

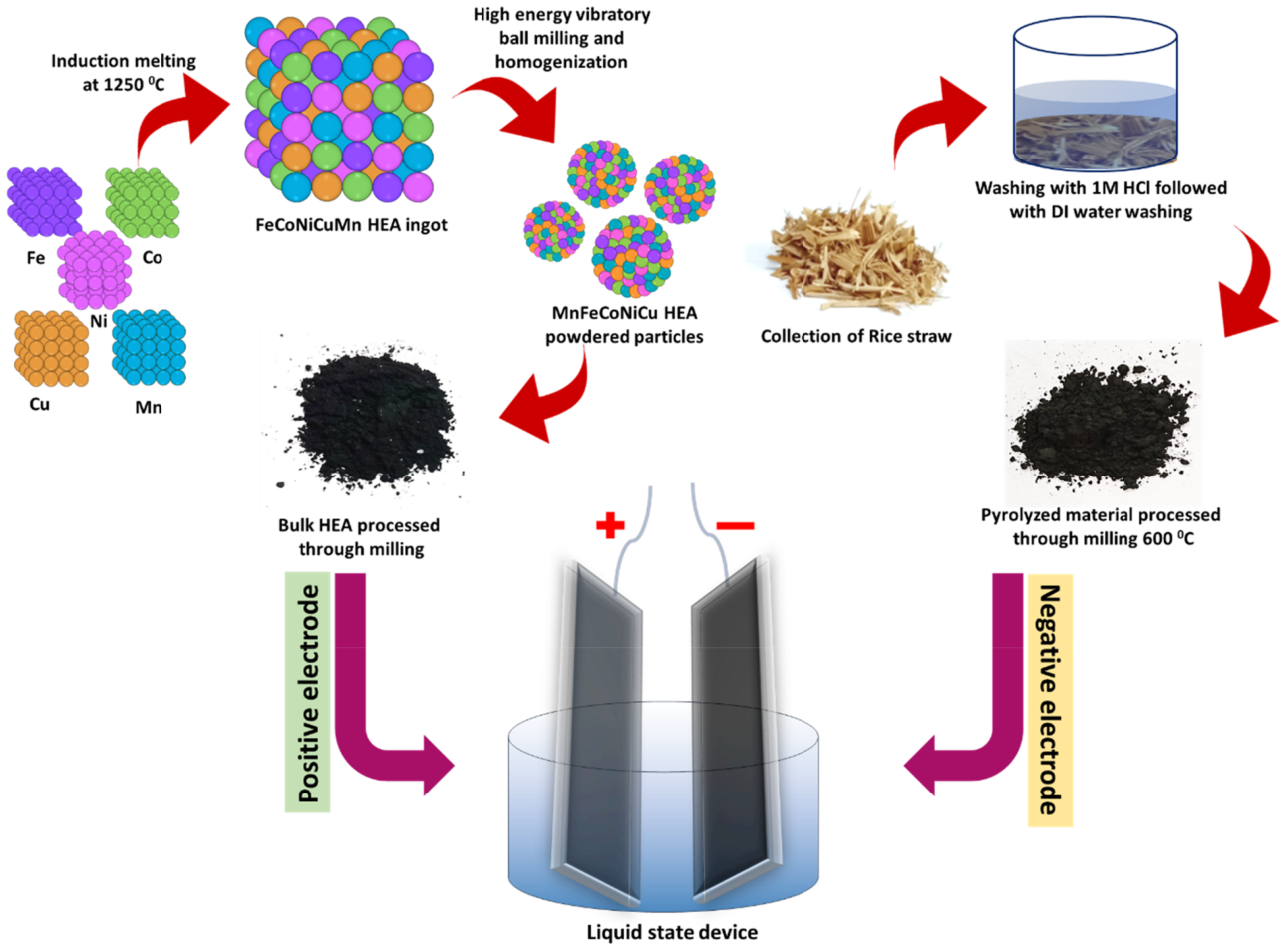

FIGURE 1 Synthesis schematic for FeCoNiCuMn HEA powder, induction melting at 1250°C and homogenized heat treatment at 1000°C for 12 h followed by high energy ball milling (for 10 h to obtained 1 g of HEA powder) and synthesis schematic of green graphene from rice straw biochar at 600°C pyrolysis, ball milled and sonicated. The HEA was used as positive and green graphene from RS-biochar as negative electrode for fabricating liquid state asymmetric device.

2 mm size range. ~2 mm sized particles were sieved and pyrolyzed at 600°C in tube furnace. Finally, the pyrolyzed material was named green graphene (GG) after vibratory ball milling for 3 h and probe sonicated for 1 h. The synthesis schematic is as shown in Figure 1.

3 | RESULTS AND DISCUSSIONS

3.1 | Structural characterizations of FeCoNiCuMn HEA

X-ray diffraction pattern of single-phase FeCoNiCuMn HEA bulk and powder is as seen in Figure 2A. Major peaks at 43.46, 50.55, 74.50, and 90.45, correspond to planes (111), (200), (220), and (311) of FCC structure.[39-41] The lattice constant is calculated to be 3.56 Å. Additionally, it has been possible to determine whether surface functional groups are present in the bulk HEA nanostructure using the FTIR spectrum from Figure 2B. Three main peaks at 530, 562, and 591 cm^{-1} are mapped. Fe-O bond vibration peak observed at 530 cm^{-1}.[42] Peak 562 cm^{-1} belongs to the asymmetric stretching of Co-O.[43] Peak 591 cm^{-1} is associated with bending vibration of Cu-O bond. The FTIR study confirmed that surface oxidized elements like Cu, Fe, and Co have significant consequence in the origin of charge storage in quinary HEA nanoparticles.

The additional surface properties of this quinary nanostructured HEA can be evaluated with BET. The Figure 2C shows N_2 adsorption-desorption curves, which form a hysteresis loop from which BET surface area was calculated to be 19.26 $m^2\ g^{-1}$. Additionally, pore size can be determined with BJH model as shown in Figure S1A, which shows the maximum number of pores in the mesoporous region (<50 nm), which contributes to increased energy density. Mean zeta potential was 14 mV as shown in Figure S1B. Positive value of zeta potential refers to stable electrostatic interaction of particles and aids stable electrochemical double layer capacitance (EDLC) layer formation.

The morphological distribution of FeCoNiCuMn HEA powder is as shown in the Figure 2D. The FESEM images clearly shows low-magnification image with a clear picture of nanoparticles agglomeration. The elemental mapping can be seen in Figure 2E-I. The Figure 2J-L shows HRTEM image with agglomerated clusters. A small section was used to understand plane distribution and further processed to obtain FFT pattern. The interplanar spacing derived from inverse FFT pattern was around 0.205 nm corresponding to the plane (111).

The survey scan in Figure S4A displays presence of all quinary elements. Deconvoluted XPS spectra of each element's oxidation states are explained in the following section. Starting with Fe 2p scan (Figure S4B), the broad peak at 711.93 eV corresponds to Fe^{2+} ($2p_{3/2}$), while the peak addressed at 725.94 eV shows Fe^{2+} ($2p_{1/2}$) of Fe2p.[44] The other peaks appear at 719.95 and 733.15 eV, addressed as Fe^0 and satellite peaks, respectively, which possess mixed valance Fe state. Also, from the deconvoluted XPS spectrum Co2p (Figure S4C), 780.89 ($2p_{3/2}$) and 796.55 eV ($2p_{3/2}$) peak ascribed to the Co^{2+} of Co2p. At the same time, other corresponding peaks, along with main peaks at 786.43 and 802.75 eV, shake up satellite peaks of Co. Similarly, Ni2p's main intense peaks split into two broad peaks at 855.46 ($2p_{3/2}$) and 873.79 eV ($2p_{3/2}$) belong to Ni^{2+} of Ni2p shown in Figure S4D. The weaker intense peak appears at 861.13 eV, corresponding to the satellite peak for Ni2p. Similarly for Cu2p in Figure S4E, the peak appears at 934.69 eV, corresponding to the Cu^{2+} of $Cu2p_{3/2}$, while Cu^{+} was addressed at 952.87 eV ($2p_{1/2}$) and 932.62 eV ($2p_{3/2}$), respectively.[45] The satellite peak appears at 942.23 eV refers to mixed valance states of surface oxidized Cu. For Mn2p as presented in Figure S4F, Mn^{3+} at 652.27 and 641.79 eV of Mn2p, while 647.50 eV and 637.56 were assigned to Mn^{4+}.[46] The broad oxygen peak appears due to the spontaneous surface oxidation of quinary HEA during ball milling in presence of oxygen.

3.2 | Structural characterizations of biochar

The Figure 3A depicts the XRD pattern of GG derived from rice straw biochar. Here, in addition to a large peak in the 2θ range of 20°-30°, the spectrum shows a few high intensity peaks with presence of carbon/graphene and graphene collective silica components. Earlier investigations reached similar conclusions for the silica-combined graphene nanocomposite along with peaks that mimic the potential presence of crystalline Si and materials based on graphene.[47] In case of green graphene, it consists of Silica rich, $Ca(OH)_2$, and C, respectively, which actively participate in the electrochemical activities. Further in cyclic voltammograms (CVs) characteristics show more pseudocapacitive behavior in lower scan rate while increasing scan rate dominance as redox activities decreases and EDLC increases. This is due to the contribution of ionic adsorption on the high specific surface area of GG. The extraordinary pseudocapacitive nature of green graphene is believed to originate from the presence of hybridized C, SiO_2,[48] and $Ca(OH)_2$.[49] This multielement characteristics of GGs actively interact with aqueous KOH electrolytes boosting specific capacitance. Also, there is intercalation deintercalation of electrolytic ions

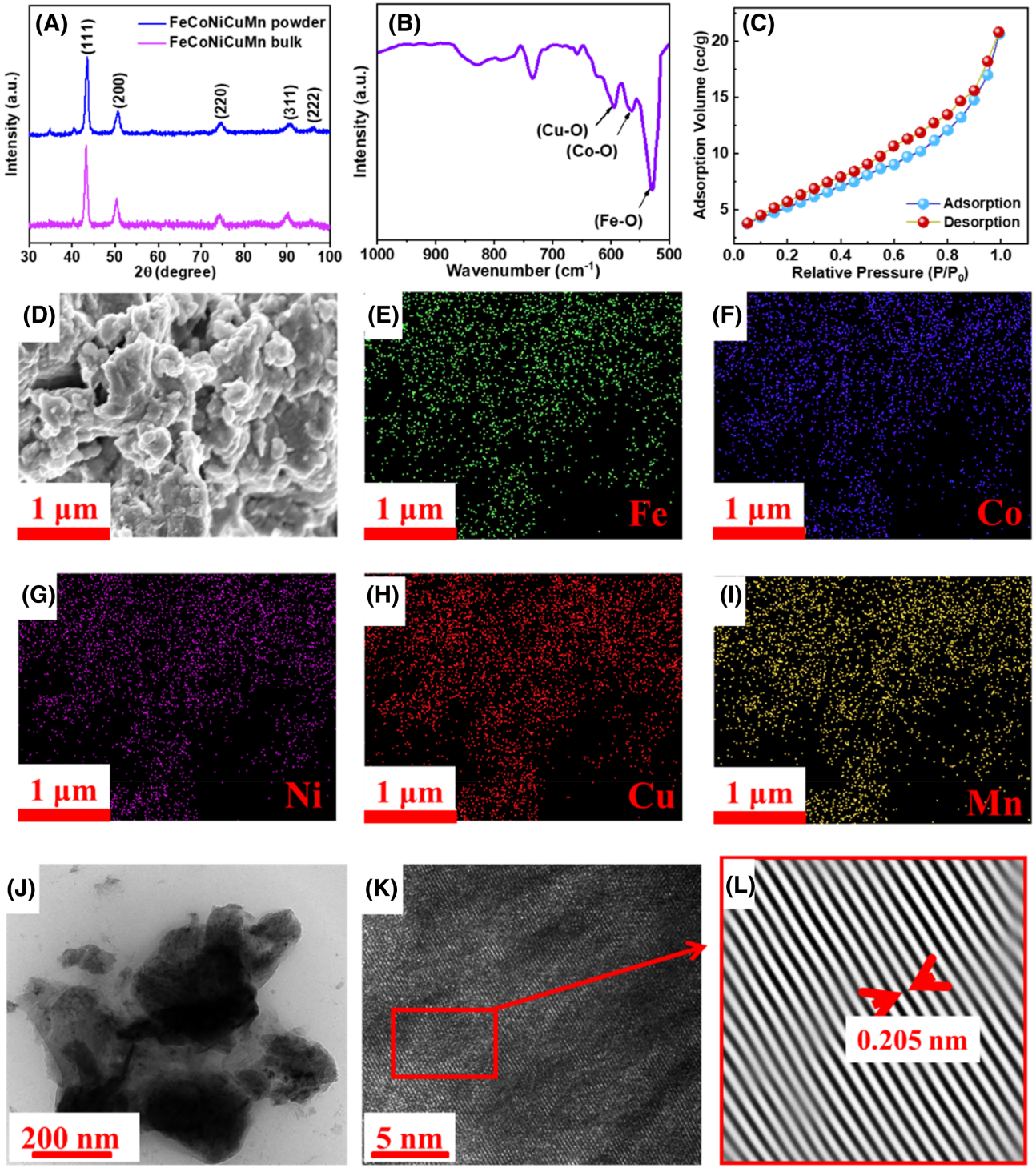

FIGURE 2 (A) XRD pattern of bulk and powder FeCoNiCuMn HEA (B) FTIR of powdered HEA (C) BET adsorption-desorption curve, (D) SEM image of HEA, (E-I) EDAX elemental mapping of all quinary elements of HEA and (J-L) HRTEM analysis followed by fringes pattern and determination of lattice spacing.

into porous layered graphitic structure resulting in the higher advanced cyclic area under CVs. FTIR spectra were used to examine the functional groups that are present in GG sheets. Figure 3B shows FTIR spectra with peaks at 463, 640, 784, 1049, and 3440 cm^{-1} confirm multiple elemental bond vibration. Peaks at 3443 and 1634 cm^{-1}, were due to aromatic C=C bonds and the -O--H stretching vibration, respectively.[50] The peaks at 780 and 1050 cm^{-1} corresponds to the symmetric and asymmetric stretching of Si-O-Si bond.[51] Furthermore, the band at 463 cm^{-1} could have originated from the bending vibration of the Si-O-Si bond.[50]

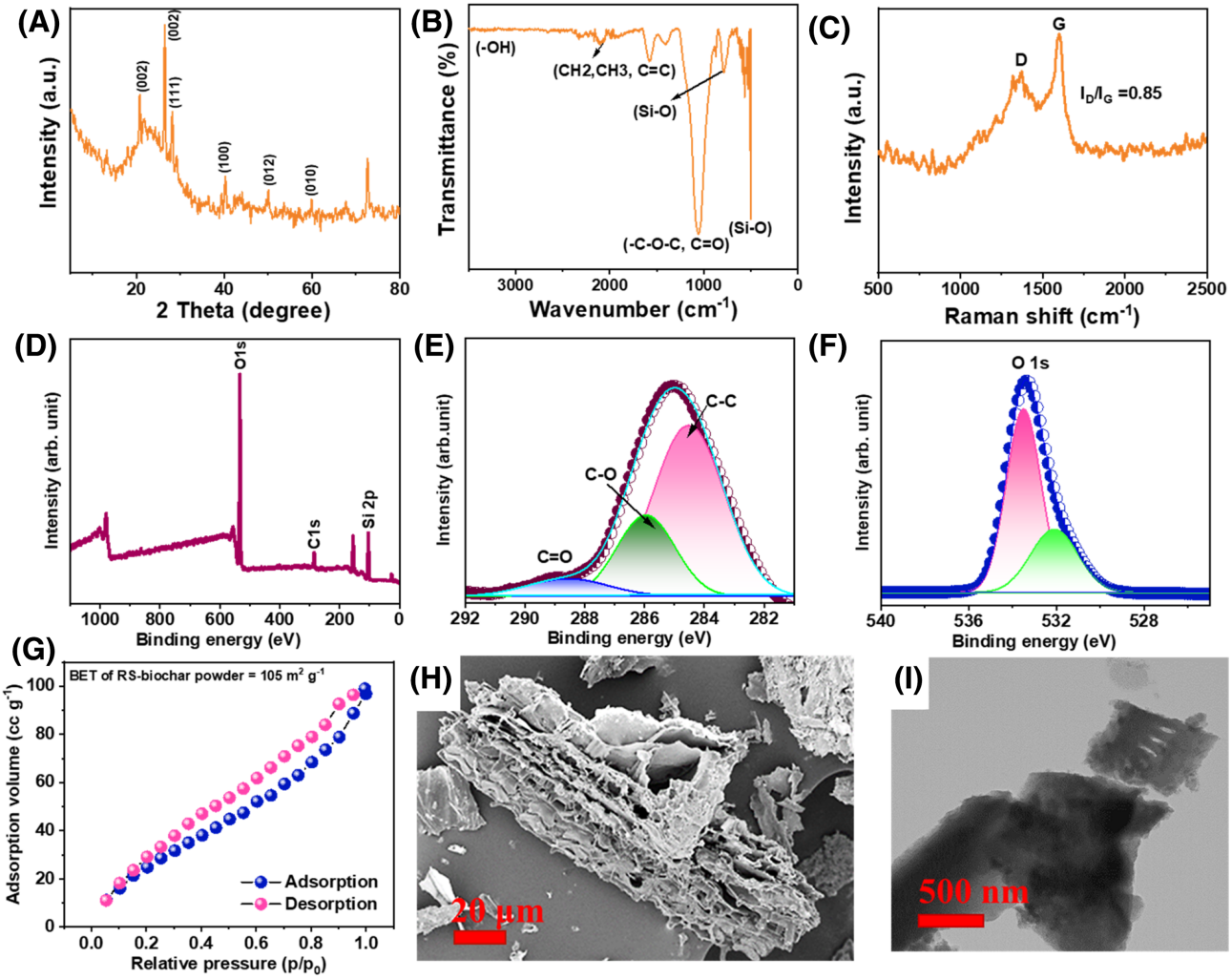

FIGURE 3 Characterization of green graphene derived from rice straw biochar (A) XRD, (B) FTIR spectrum, (C) Raman spectra, (D-F) XPS analysis, (G) BET plot, (H) FESEM image, and (I) HRTEM image.

Raman analysis was used to identify the presence of defective and graphitic bands to understand how the graphene-based structures evolved. As seen in Figure 3C, The D and G bands are determined by the Raman spectra band at 1344 and 1582 cm^{-1}, respectively. Narayanan et al.[51] claims that the sp^2 carbon structure, indicates the G-band a property of graphitic materials. However, the D bands were observed due to imperfections of sp^3-hybridized carbon. The above peaks' ratio of I_D/I_G was 1, which revealed the occurrence of a layered graphitic structure. The TEM image in Figure S8A,B shows layered structures with different planes and its FFT pattern. The Figure 3D shows XPS survey of GG. The survey plot shows all primary elements C, Si, and O being present. Further deconvoluting the C and O peaks shows a clear characteristic of graphitic structures. In the Figure 3E the deconvoluted peaks of C1s appear at 284.52, 285.95, and 288.57 eV, refers to the conjugate bond (C-C), carbonyl (C-O), and carboxyl group (C=O) of C1s, respectively.[52,53] Hence the orbitals associated with C1s are mostly sp^3 hybridized, and the remaining C orbitals are constructed the C-O and O-C=O. The deconvoluted peaks of O1s at 532.2 and 533.48 eV as shown in Figure 3F, corresponds to the C-O and C=O, which confirm strong interaction of C and O atom in the GG derived from rice straw biochar.[52,54]

The BET analysis was used to observe the prepared GG sheets with various surface kinetics, pore volume as well as pore distribution. For the analysis, a test was performed at 77 K using N_2 physical adsorption tests, and the obtained result is as shown in Figure 3G. Obtained BET graph of GG sheets were classified as a type-II curve, and exhibited increased adsorption with a minor N_2 sorption profile. It was observed due to cellulose, hemicellulose, and lignin decomposition in the mesoporous channels. However, at relative pressures of 0.8 and 1.0, noticeable increase in N_2 sorption characteristic was also observed, indicating that GG sheets may have a

microporous structure.[55] Surface area of GG sheets was 7.3 $m^2 g^{-1}$, and the mean pore diameter was reported to be very similar to 4.6 nm.[55] Additionally, pore volume of 7.4 $cm^3 g^{-1}$ was noted and pore size distribution also noted along noted at Figure S1C.

The Figure 3H shows a FESEM image of rice straw biochar. The images show a clear porous graphitic structure obtained after ball milling of biochar. The three-dimensional macroporous networks help strong electrochemical activities and boost pseudocapacitive performance. HRTEM shows the agglomerated graphitic structure as seen in Figure 3I. The surface electrostatic charge GG is demonstrated with help of zeta potential. As shown in Figure S1D, the mean zeta potential was −24 mV. The electrophoretic mobility of both green graphene and HEA is as shown in Figure S1E. The negative value of zeta potential has significant contribution in negative potential range CV as shown in Figure 4A, which attributes a stable EDLC characteristics in the surface of GG electrode. Additionally, particle size

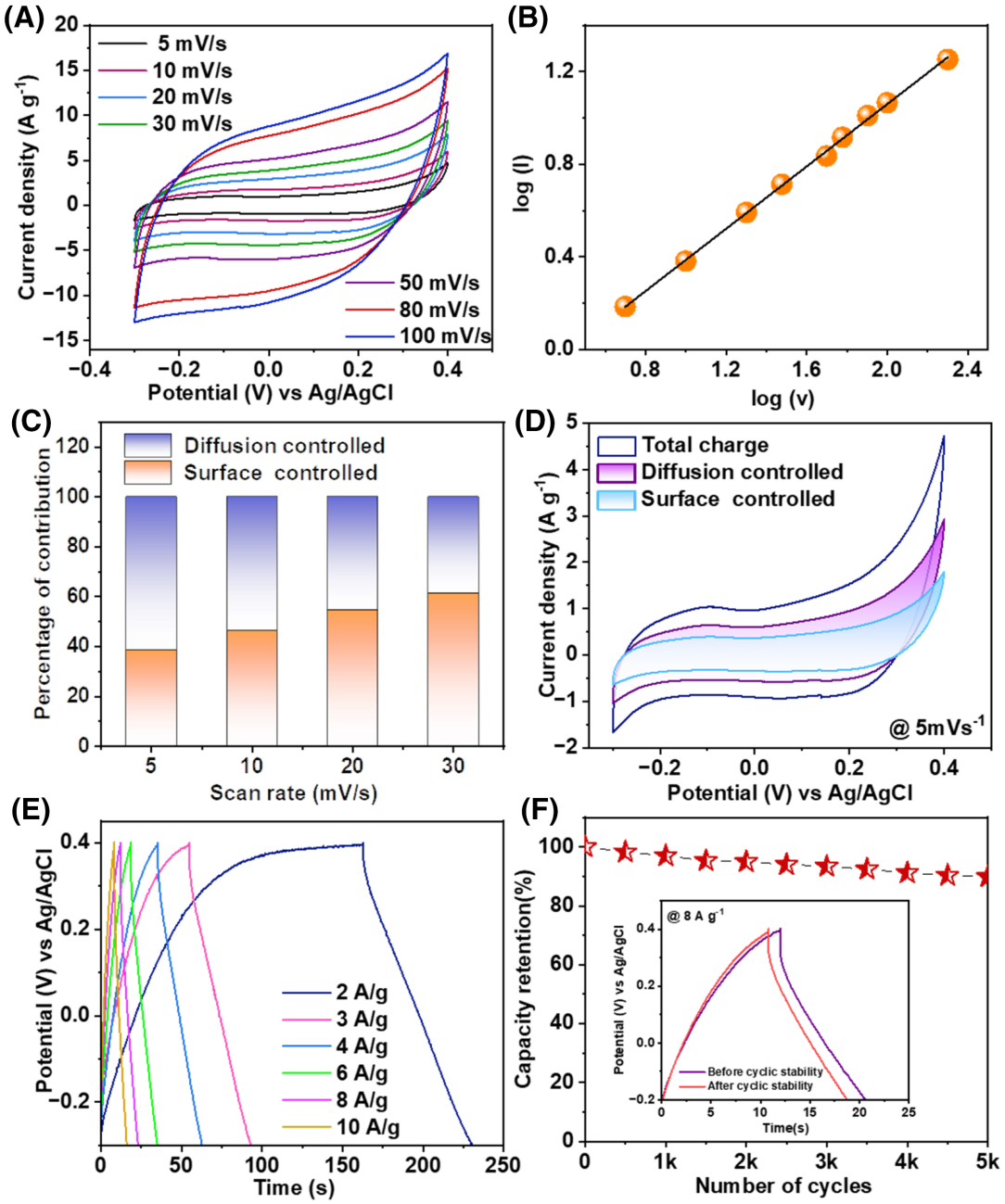

FIGURE 4 (A) CV graphs at different sweep rates 5 to 100 mV s^{-1}, (B) log (I) vs log (ν) at 0.2 V around 0.673, (C) Percentage quantified for each sweep rate, (D) Current response at 5 mV s^{-1} for both the surface controlled and diffusion controlled mechanism, (E) GCD plots for the HEA electrode, and (F) Cyclic stability at 8 A g^{-1} up to 5000 cycles.

distribution is obtained by DLS with average hydrodynamic size 30 μm of the porous graphite structure.

4 | SUPERCAPACITOR PERFORMANCE OF ELECTRODES

Optimized 3 M KOH aqueous electrolyte is used to demonstrate the electrochemical performance of the FeCoNiCuMn HEA electrode. Due to its maximum ionic conductivity with smaller hydrated ionic sizes, the selection of KOH electrolyte participates in greater ionic interaction activities. Additionally, previous studies back the selection of alkaline electrolytes for FeCoNiCuMn HEA and GGs (biochar) electrodes. Among various concentrations of KOH, 3 M KOH shows greater supercapacitive performance, so further electrochemical characterizations are taken in 3 M KOH electrolytic concentration (Figure S2A). CV curves of the FeCoNiCuMn electrode are shown in Figure 4A taken in between scan rates ranging from 5 to 200 mVs^{-1}. The lack of redox peaks in CV curves indicates that EDLC activities predominate on the electrode surface, with a lesser degree of slow diffusion-controlled faradic mechanism. Also, quinary elements with respective surface oxidations contribute to non-rectangular CV structures.

Furthermore, the dominance of CV area in the negative potential window is mainly due to the presence of Fe and Mn. In contrast, Ni, Co, and Cu are the capacitive elements that contribute to the positive potential window. Hence, choosing multivalent quinary HEA with different transition elements can exhibit a greater potential window in both positive and negative directions. From the nature of CV, both half cycles' peak current (both reduction and oxidation peak) has a relationship with sweep rate (ν), which can be expressed as $I = a\ \nu^{b}$[56] where constants 'a' and 'b' are modifiable, which provide inside kinetics of charge storage. The constant 'b' value ranging from 0.5 to 1 signifies pure faradic to pure EDLC behavior, respectively. The exact value of 'b' can be evaluated from the slope of log (I) and log (ν) at 0.2 V as seen in Figure 4B. The value $b = 0.73$ indicates both slow faradic and EDLC contributions combined.

The pore size distribution plays an important role for electrolytic ion participation in both surface controlled and diffusion controlled process. Supercapacitors can store charge by two mechanisms briefly explained as EDLC surface controlled and slow diffusion controlled faradic mechanism, which is expressed as relation in the form of $q_{total} = q_s + q_d$, q_s is amount of charge stored by surface controlled process while q_d refers amount of charge stored by diffusion controlled process, the value of q_s can be estimated[57] from the total charge axis intercept using the formula 'q_t' vs '$\nu^{-1/2}$' plot from the Figure S2B. At each scan rate, we deduce the intercept from the total charge in order to evaluate both contributions. Figure 4C shows the relative contribution in percentage of q_s and q_d at different scan rates. It is observed that with increasing scan rate, the diffusion-controlled faradic process decreases due to surface adsorption mechanism. This demonstrates that as the sweep rate is increased, surface ion adsorption increases and the electrode material has more time to participate in surface intercalation and deintercalation at a lower scanning rate. Thus, the changes in oxidation state is associated with multivalent transition metal quinary elements in fast faradic surface redox reactions.

Also, a second analysis can be employed to emphasize a more quantitative interpretation of CV from which individual current contribution of above mentioned mechanisms can be explained. The total current response of the electrode with each scan rate dependency is expressed by Dunn and co-researchers with the relation[58]:

$$i = k_1\nu + k_2\nu^{1/2} \tag{1}$$

$$\frac{i}{\nu^{1/2}} = k_1\nu^{1/2+k_2} \tag{2}$$

Here, the parameters $k_1\nu$ and $k_2\nu^{1/2}$ represent current distribution associated with surface-controlled and slow diffusion-controlled processes, respectively. Where k_1 and k_2 are adjustable constants that can be estimated using the plot of $\frac{i}{\nu^{1/2}}$ against $\nu^{1/2}$. As shown in Figure 4D, the current contribution from the diffusion-controlled process ($k_1\nu$) of the FeCoNiCuMn electrode can be estimated from the overall current distribution using Equations 1 and 2. According to the aforementioned analysis, 62% of the total current response, or more than the total current response, is contributed by the semi-infinite linear diffusion process. However, as seen in the same Figure 4D, surface-controlled capacitive contribution accounts for 38% of the total current response, which is easily estimated using the relation mentioned above. This increased slow diffused faradic activities in FeCoNiCuMn electrode at lower scans might also be the origin of electrolytic ion interaction with redox active sites. Also, with increasing scan rate, surface-controlled mechanism dominance is observed. Now calculating C_s from CV curves using Equation S1. Highest C_s obtained 388.28 $F\,g^{-1}$ at a lower scan rate region (5 $mV\,s^{-1}$) while increasing sweep rate capacitance exponentially decays to 55% of the initial value at 200 $mV\,s^{-1}$.

Furthermore, in-depth electrochemical analysis can be verified using GCD plots taken for FeCoNiCuMn

electrode. The GCD plots (as shown in Figure 4E) of this quinary HEA electrodes are a nonlinear characteristic due to deep interaction with K^+ ions of aqueous KOH electrolyte. With its dual charge storage singularities having spontaneous surface oxidation properties, the electrode gives a good current response over time. For FeCoNiCuMn HEA, C_s was calculated using Equation S2, around 194 F g^{-1} at 2 A g^{-1}. With increased current rate to 10 times, C_s drops to 60%. The surface oxidized HEA nanoparticle shows comparable results with transition metal combination due to synergistic behavior of all elements in HEAs. The cyclic stability of FeCoNiCuMn HEA electrode is demonstrated at 8 A g^{-1} up to continuous charge-discharge cycle as shown in Figure 4F. The capacity retention dropped to 92.3% after 5000 cycles and remained stable, which provides a suitable electrode material for supercapacitor application. Further insight into electrochemical kinetics of the FeCoNiCuMn and GG electrode in respective single electrode system studies. The Figure S2C shows Nyquist of FeCoNiCuMn HEA electrode taken between the frequency ranges of 1 to 10 kHz. The lower value of R_s around 3.5 Ω suggests good supercapacitive characteristics and constant phase eliminator was inclined. Figure S2D shows EIS fitted curves of the HEA electrode.

The C_s obtained for FeCoNiCuMn HEA electrode at 5 mV s^{-1} was 388.28 F g^{-1} and 195 F g^{-1} at 2 A g^{-1} demonstrated at 3 M KOH aqueous electrolyte. The C_s is quite reasonable and comparable with respect to some of our previous HEA studies with FeCoNiCuZn[59] and FeCoNiCrMn[60] HEAs and other HEAs as shown in Table 1. The higher specific capacitance FeCoNiCuMn HEA electrode due to their multivalent quinary elements with multiple states contributing such as: Fe^{2+}, Fe^{3+}, Ni^{2+}, Mn^{3+}, Mn^{4+}, Co^{2+}, and Cu^+ with their respective surface oxidations backing these capacitive results.

Next, the GG electrode's supercapacitive performance can be explained in a similar manner as FeCoNiCuMn HEA electrode. The CV scans are recorded in between scan range of 5 to 200 mV s^{-1}, potential window of −1.0 to 0.0 V (Figure 5A). The CVs shape characteristics are more pseudocapacitive behavior in lower scan rate while increasing scan rate dominance of redox activities decreases and EDLC increases, due to the contributor through ion adsorption on the high specific surface area of green graphene. This extraordinary pseudocapacitive nature of GG may be due to the presence of hybridized C, SiO_2,[48] and $Ca(OH)_2$.[49] This multielement characteristic presence in GGs actively interact with aqueous KOH electrolytes boosting specific capacitance. Also, there is intercalation-deintercalation of electrolytic ions into porous layered graphitic structure resulting in higher advanced cyclic area under CVs.

In detail, quantification of "surface controlled" and slow infinite "diffusion controlled" capacitance was estimated from the above relation and the total charge (obtained from the cyclic area) and sweep rate is as shown in Figure 5B. For a clear understanding, the percentage of contribution with respective scan rate is employed in Figure 5C. We note that the redox phenomena can be explained with lower scan rate considering 5 mVs^{-1}, the slow faradic diffusion controlled dominance is higher than surface adsorption. While increasing scanning rates at 50 mVs^{-1}, the diffusion-controlled characteristics was significant due to redox activities with KOH electrolyte. The additional result of charge transfer depends on how electrode material interacts with active electrolytic ions. Also, as shown in Figure 5D,E, a separate current response over the total current for a particular scan rate 5 mVs^{-1} is calculated using the Equations (1) and (2).

Conversely, GCD plots of GG followed a strong faradic behavior with more plateaus in lower current rates, mimicking properties of various redox materials, proving excellent supercapacitive behavior (Figure 5F). Highest C_s was obtained at 2 A g^{-1} is around 410 F g^{-1} by using Equation S2. Though the current density was improved up to six times, the C_s drops 60% of initial value, proving the electrode material's practical charge storing applicability. The single electrode cyclic stability also demonstrated up to 5000 cycles (Figure 5H). The capacity retention of 97.8% proves excellent capacity retention. Figure 5I shows GCD before and after cycling. In further comparison with rice straw based supercapacitors[68-70] this silica rich GG derived from rice straw gives prominent specific capacity. In similar fashion EIS analysis of the GG electrode is shown in Figure 5G above which mimics same circuit pattern of a series resistance along with a constant phase eliminator, which is taken in between frequency range of 100 kHz to 1 Hz. We have compared some of the existing agricultural derived carbon biomass supercapacitors as shown in Table 2.

4.1 | Asymmetric liquid state device study

For a supercapacitor device, asymmetric devices have good performance due to increased operating potential window, higher energy density, and long-term cyclic stability. The asymmetric liquid state device is fabricated with FeCoNiCuMn HEA as positive and GG as negative electrodes. To get the best performance, the charge-balanced mass loading is taken in both electrodes.[88] The required mass loading on both electrodes was calculated with the assistance of the charge balance equation, as

TABLE 1 Comparison of this FeCoNiCuMn HEA with various HEA based electrode.

Electrode material	Synthesis method	Morphology	Electrolyte	Potential window	Specific capacitance	Ref.
$(CrMnFeCoNi)_3O_4$	Co-precipitation	Quasi spherical	2 M KOH	0.0 to 0.45 V	239 F g^{-1} @0.5 A g^{-1}	24
$(FeCoCrMnZn)_3O_4$	Solid state reaction	Irregular particles and agglomeration	1 M KOH	0.15 to 0.5 V	340.3 F g^{-1} @ 0.5 A g^{-1}	25
AlCoCrFeNi two phase dissolution	Selective phase dissolution	Nanoporous structure	2 M KOH	−0.2 to 0.5 V	700 mF/cm^2 at 1 mA/cm^2	26
FeNiCoMnMg HEA-NPs/ACNFs	CTS method	Nanoporous structure	6 M KOH	0.0 to 0.8 V	203 F g^{-1}@ 1 mA/cm^2	27
HEA-NP@MOL/HCPC	Liquid phase synthesis	Cluster of nanoparticles	1 M KOH	−1.0 to 0.0 V	495.4 F g^{-1} at 0.5 A g^{-1}	61
rHEO−CNT	Solgel method	Connected nanoparticles in nanotubes	1 M H_2SO_4	0.0 to 1.0 V	157.5 F g^{-1} at 1 A g^{-1}	28
HEA-Nitrides	Mechanochemical assisted synthesis	Nano flakes architecture	1 M KOH	−1.0 to 0.0 V	230F g^{-1} at 10 mV s^{-1}	62
(TiNbTaZrHf)C powder	Facile electrochemical process	Spherical nanoparticles	1 M KOH	−1.0 to 0.0 V	95.2F g^{-1} at 10 mV s^{-1}	63
(VNbTaZrHf)C	Direct electro-deoxidation	Dense block structure	1 M KOH	−0.7 to −0.2 V	151 F g^{-1} at 10 mV s^{-1}	64
HEO/f-CSAC	Grinding	Cavity-type microstructure	1 M NaCl	0.0 to 1.0 V	147.5F g^{-1} at 1 A g^{-1}	29
$(Zr_{0.5}Ti_{0.5}Ce_{0.5}Hf_{0.5})O_7$	Sol-Gel synthesis	Roughly rice-like	1 M Na_2SO_4	−1.0 to 1 V	703.3 F g^{-1} at 1 A g^{-1}	65
NiCuFeCoMn-Carbonate	Hydrothermal Method	Structure flowers like	1 M KOH	0.1 to 0.5 V	1241 F g^{-1} at 3 A g^{-1}	30
$La_{0.7}Bi_{0.3}Mn_{0.4}Fe_{0.3}Cu_{0.3}O_3$ HEP	Solvothermal	Spherical shell pore structure	6 M KOH	−1.0 to 0.0 V	480.95 C g^{-1} at 0.5 A g^{-1}	66
$K(MgMnFeCuNi)Fe(CN)_6$	Mechanochemical	Agglomeration particles	1 M Na_2SO_4	0.2 to 1.0 V	175 F g^{-1} at 5 mVs^{-1}	67
CoCrNiFeMn HEA	Induction melting, ball milling	Agglomeration nanostructure	3 M KOH	−0.1 to 0.5 V	264 F g^{-1} at 1 A g^{-1}	60
FeCoNiCuZn HEA	Induction melting, ball milling	Nanostructured agglomeration	3 M KOH	0.0 to 0.5 V	325.17 F g^{-1} at 1 A g^{-1}	59
FeCoNiCuMn HEA	Induction melting, ball milling	Agglomeration nanostructure	3 M KOH	−0.3 to 0.4 V	194 F g^{-1} at 2 A g^{-1}	This study

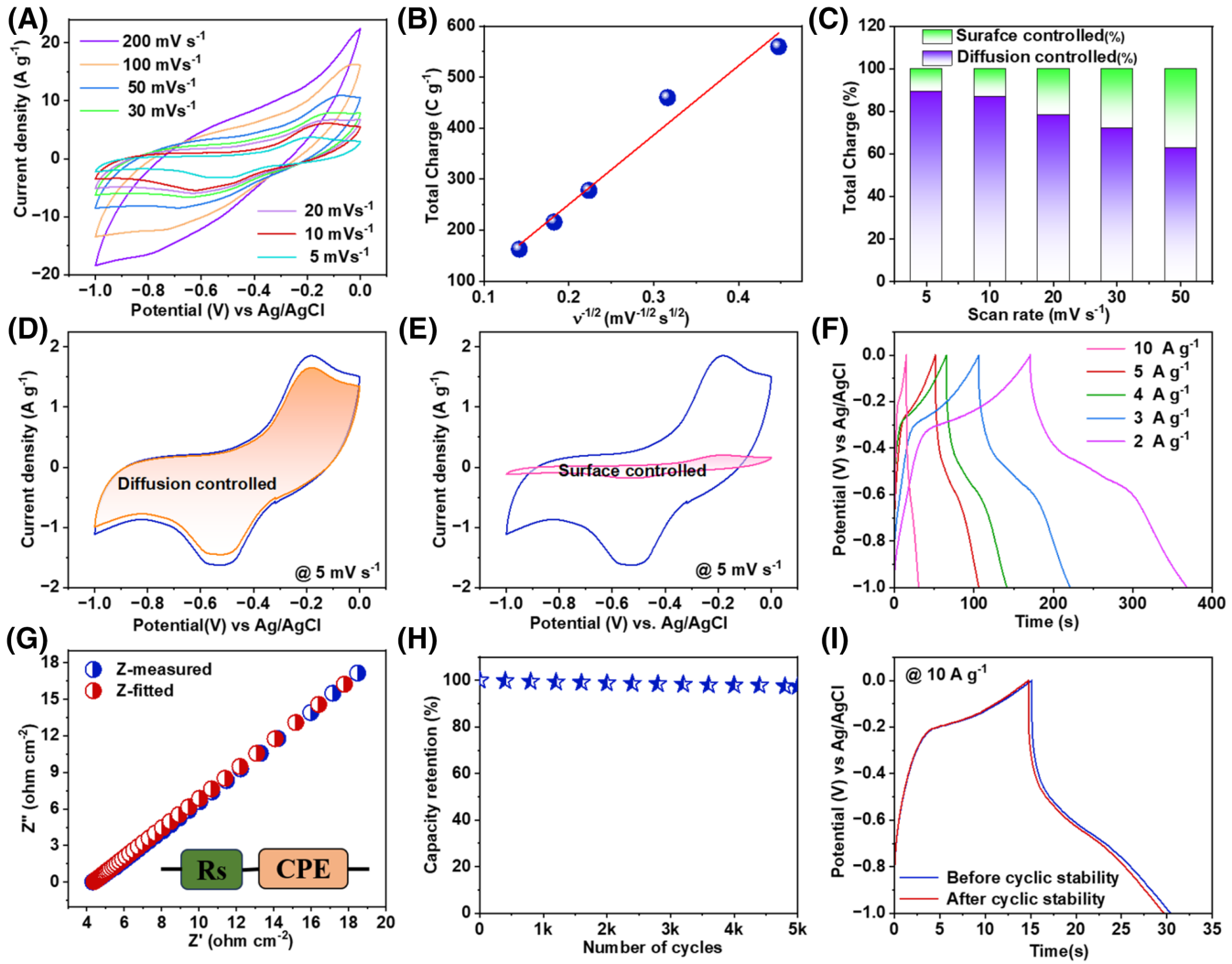

FIGURE 5 (A) CV at different scan rates (5-200 mV s^{-1}), (B) Total charge (q) vs inverse square root of scan rate, (C) Percentage contribution of both q_s and q_d mechanism for various scan rate 5 to 50 mV s, (D, E) diffusion controlled and surface controlled current contribution to the total current at 5 mV s^{-1}, (F) Charge discharge at different current density, (G) Nyquist plot for GG electrode, (H) Cyclic stability of GG electrode at 10 A g^{-1} up to 5000 cycles, and (I) GCD of GG before and after cyclic stability.

shown in the Equations S3 and S4. The Figure S3A shows the CV of FeCoNiCuMn HEA and GG electrode at 5 mV s^{-1} from which respective C_s was calculated. Putting respective C_s, m, and V, the ratio was 2.0. To create an asymmetric liquid state device, 1 mg of FeCoNiCuMn HEA and 0.5 mg of GG were considered.

Figure 6A shows CV stability optimized up to 1.7 V at 50 mVs^{-1}, showing no discontinuities, even with increasing voltage window 0.8 to 1.7 V. Characteristic cyclic area under CV increases continuously concerning looping the lower CV areas. This promises a clear understanding of the advantages of demonstrating the ASC device. Further CV scans are recorded in between 5 and 200 mV s^{-1} within the 0 to 1.7 V potential range, as demonstrated in Figure 6B. Here from the nature of CV, it was observed that shapes are neither pure rectangular nor pure redox type. This concludes a mixed response for HEA and GG as a form of pseudocapacitive (in association with ion intercalation and deintercalation) and EDLC type nature, respectively. This asymmetric combination of both electrode materials leads to the increased area under CV, giving a C_s of 114 to 61 F g^{-1} in scan rate ranging from 5 to 100 mV s^{-1} with a slow charge storage kinetics and fast cyclic reversibility. In addition, the GCD curves were also measured between the current density range of 2 to 10 A g^{-1} with same voltage stability the of 0 to 1.7 V, as seen in Figure 6C. Mimicking the nonlinear characteristics at lower current rate while increasing the scan rate, the GCD curves become more triangular. Further evaluating C_s, we obtained 83.22 F g^{-1} at 2 A g^{-1} with increasing

TABLE 2 Comparison of green graphene from RS-biochar with various agricultural derived carbon biomass supercapacitors.

Carbon sources	Pyrolysis activation techniques	Morphology	Electrolyte/potential window (V)	Specific capacitance	Ref.
Peanut shells	Calcined in a furnace 800°C	Worm-hole-like pores	1 M KOH −0.5 to 0.5	136 F g^{-1}@ 2 A g^{-1}	71
Wolfberry fruits	Catalytic carbonization/$Sncl_2$	Blanket-like rough structure	6 M KOH −1.0 to 0.0	365 F g^{-1}@ 0.2 A g^{-1}	72
Chestnut pulp	Carbonization	Pseudo-honeycomb-like 3D network	6 M KOH −1.0 to 0.0	373 F g^{-1} @ 0.5 A g^{-1}	73
Cornstalk	800°C carbonization	Three-dimensional mesh-like pore	6 M KOH −1.0 to 0.0	350.4 F g^{-1} @0.2 A g^{-1}	74
Wheat straw	Microwave heating 500°C	Interconnected macropores	6 M KOH −1.0 to 0.0	325 F g^{-1} @ 0.5 A g^{-1}	75
Discarded tea waste	700°C carbonization	Bulk flakes densely packed structure	3 M KOH −0.8 to 0.3	131.95 F g^{-1} @0.5 A g^{-1}	76
Cherry stones	700°C carbonization	Large pore structure	6 M KOH −1.0 to 0.0	370.5 F g^{-1} @ 0.5 A g^{-1}	77
Corncob waste	750°C carbonization	Uniform porous structure	6 M KOH −1.0 to 0.0	394.9 F g^{-1} @ 1 A g^{-1}	78
Wheat husk	800°C carbonization	Hollow tunnel's structure	6 M KOH −1.0 to 0.0	271.5 F g^{-1} @ 0.5 A g^{-1}	79
Rice straw	400°C carbonization	Mesoporous structure	6 M KOH −1.0 to 0.0	324 @ 0.5 A g^{-1}	80
Garlic seeds	700°C carbonization	Porous honeycomb-like structure	6 M KOH −1.0 to 0.0	268 F g^{-1} @ 0.5 A g^{-1}	81
Willow wood	800°C carbonization	Microporous structure	6 M KOH −1.0 to 0.0	394 F g^{-1} @ 1 A g^{-1}	82
Waste Bagasse	700°C carbonization	Porous structure	6 M KOH −1.0 to 0.0	455 F g^{-1}@ 0.5 A g^{-1}	83
Taro epidermis	800°C carbonization	Cambered sheet structure	6 M KOH −1.0 to 0.0	466 @ 1 A g^{-1}	84
Pine nut shells	600°C carbonization	Interconnected carbon nanosheets	6 M KOH −1.0 to 0.0	-	85
Crab shells and rice husks	700°C carbonization	3D hierarchically porous structure	6 M KOH −1.0 to 0.0	474 F g^{-1} @ 0.5 A g^{-1}	86
Bean dregs	500°C carbonization	Porous structure	6 M KOH −1.0 to 0.0	197 Fg^{-1} @ 0.3 A g^{-1}	87
Rice straw	600°C carbonization	Graphitic structure	3 M KOH −1.0 to 0.0	410 F g^{-1} at 2 A g^{-1}	This study

current rate 10 times capacity drop to 68.06% of the initial value (Figure 6D). Additionally, due to the improved potential window, it is important to evaluate the specific energy and power densities. Since the GCD pattern follows on linear charge discharge characteristics,[89,90] the respective energy density and power density can be calculated using the following equations.

$$E\left(\mathrm{Wh\,kg^{-1}}\right) = \frac{I\int V\,dt}{m} \tag{3}$$

$$P\left(\mathrm{W\,kg^{-1}}\right) = \frac{E}{\Delta t} \tag{4}$$

Specific energy densities calculated from the above equations are 33.4, 31.81, 30.14, 28.71, 24.22, and 22.73 Wh kg^{-1} with power densities of 1.7, 2.5, 3.4, 4.2, 6.37, and 8.5 kW kg^{-1}, respectively, as seen in the Ragone plot (Figure 6E). The higher energy density as well as higher power density results to form ASC device proves the combing results of FeCoNiCuMn and

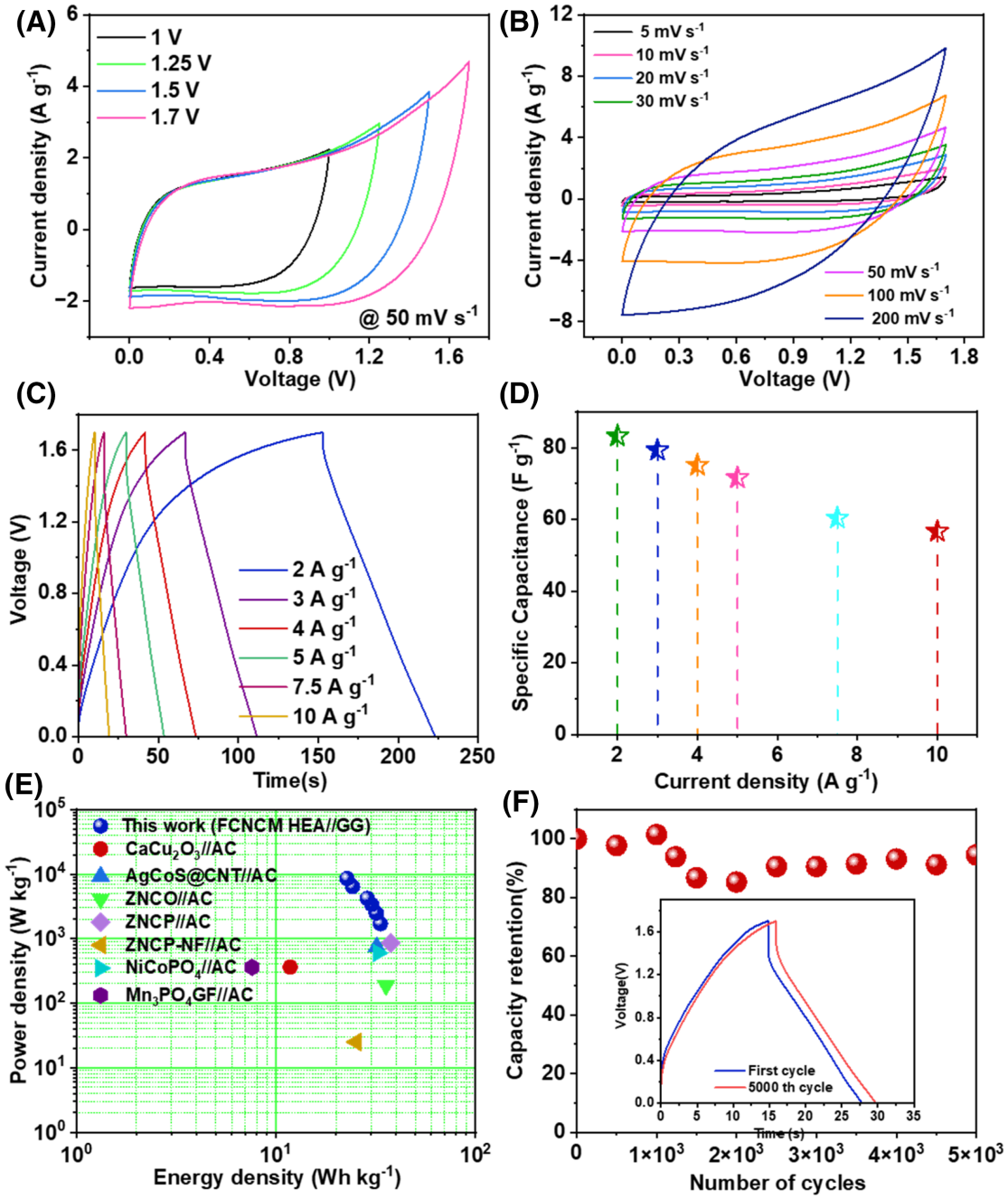

FIGURE 6 (A) CV response at different voltage window, (B) CV at different scan rate between 0 and 1.7 V, (C) GCD curves at current density ranging from 0 to 1.7 V, (D) Cs vs current density, (E) Ragone plot with comparison with different asymmetric devices, and (F) Cyclic stability at 7.5 A g^{-1} (inset first and 5000th GCD cycle).

Si-rich GG as more redox species to subsidize additional faradic pseudocapacitance to total C_s of the device. Additionally, cyclic stability was tested up to continuous charge-discharge 10000 cycles at 7.5 A g^{-1} (Figure S7). In Figure 6F, during first 1000 cycles the capacity retention remains stable with 97.4% at 500 cycle and 101% thereafter. While further increasing the cycles, the capacity drops up to 2000 cycles and further a steady retention on progressive cycles and observed 93% to 94% with charge discharge cycle reach at 5000 thereafter. The initial and final GCD curves inserted in the Figure 6F, which shows both the cycles are symmetrical in nature proves the nature of charge storage kinetics remains unaltered even after continuous charge-discharge cycle. This proves a practical utility of ASC device for long term applications which combines the properties of multivalent quinary elements of HEA nanostructure and GG. We also compare

the device results with other state-of-art supercapacitors available in Table 3.

EIS recorded between 100 kHz and 1 Hz can be used to explain electrochemical activity. The Nyquist plot is shown in the Figure S3B,D, along with fitted data. The circuit is modified using a Randal circuit with a series resistance (R_s), charge transfer resistance (R_{ct}) as well as a load resistance along with the two constant phase eliminators (CPE). The equivalent R_s value is calculated from the real impedance axis intercept which was 8 Ω. At the same time, R_{ct} is represented by the semicircle's diameter, which is approximately 5 Ω. The lower the value of R_s the greater the ion facilitation phenomenon. Low intrinsic resistance of electrode material as well as good contact between current collector/electrode material was observed.[91] The value of R_{ct} signifies fast redox activities associated with ASC device to perform better electrochemical activities. Two constant phase eliminators attributed from semi-infinite diffusion of electrolytic ions on to the electrode material. The capacitance component as well as bode plots are also displayed in Figure S3C,E. We also performed measurements for symmetric device using GG and compared the result with the FeCoNiCuMn HEA//GG asymmetric device (details in Figure S6).

4.2 | Theoretical studies

Different AI based machine learning tools have also been explored in the field of computational methodology for data collection, interpretation, algorithm selection as well as model optimization for the field.[102] The *d*-band center approach was utilized to create the equimolar concentration of a 13-atom high entropy alloy nanocluster containing the elements Fe, Co, Ni, Cu, and Mn.[103] The average *d*-band center values for individual 13-atom nanocluster are listed in Table 4. Here, the Fermi level is adjusted to zero. Mn > Ni > Fe > Co > Cu is the sequence in which the *d*-band center values of individual atoms are closest to the Fermi level. Therefore, the ratio of each kind of atoms to total atoms is 3:3:3:2:2, respectively.

With the increase in *d*-states near the Fermi level, the supercapacitance is also enhanced.[104] Density of states

TABLE 3 Various liquid state devices with this FeCoNiCuMn//GG asymmetric device.

Electrode material	Device type	Specific capacitance (F g^{-1})	Electrolyte	Energy density (Wh kg^{-1})	Power density (W/kg)	Cyclic stability	Ref.
$CaCu_2O_3$//AC	Asymmetric	40.41 F g^{-1} at 1 A g^{-1}	3 M KOH	11.8	362.5	94% after 10 k cycles	[92]
AgCoS@CNT//AC	Asymmetric	65 F g^{-1} at 1 A g^{-1}	1 M KOH	32	750	82% after 5 k cycles	[93]
$Ni_xCo_{1-x}P_{-2.5}$//AC	Asymmetric	115.8 F g^{-1} at 1 A g^{-1}	2 M KOH	31.52	700	98.3% after 10 k cycles	[94]
$Mn_3(PO_4)_2$ GF//AC	Asymmetric	28 F g^{-1} at 1 A g^{-1}	6 M KOH	7.6	360	96% after 10 k cycle	[95]
ZNCO//AC	Asymmetric	113.9 F g^{-1} at 1 A g^{-1}	6 M KOH	35.6	187.6	90% after 3 k cycles	[96]
ZNCP-NF//AC	Asymmetric	181.6 C g^{-1} at 0.2 A g^{-1}	3 M KOH	37.59	856.52	92.68% after 5 k cycles	[97]
Ni-Co-PO_4//AC	Asymmetric	162.8 F g^{-1} at 1 A g^{-1}	3 M KOH	32.5	600	80.4% after 5 k cycles	[98]
$NiCo_2O_4$@MnO_2// AC	Asymmetric	112 F g^{-1} at 1 mA cm^{-2}	1 M NaOH	35	163	71% after 5 k cycles	[99]
$CoMoO_4$@$NiMoO_4$// AC	Asymmetric	-	2 M KOH	28.7	262	99% after 3 k cycles	[100]
MnO_2/rGO//AC	Asymmetric	45.25 F g^{-1} at 0.25 A g^{-1}	1 M Na_2SO_4	25.14	250	-	[101]
FeCoNiCuMn//GGs	Asymmetric	83.22 F g^{-1} at 2 A g^{-1}	3 M KOH	33.4	1700	94% after 5 k cycles	This study

TABLE 4 *d*-band center values.

S. No.	Element	*d*-band center (eV)
1.	Fe	−7.88
2.	Co	−8
3.	Ni	−7.46
4.	Cu	−8.23
5.	Mn	−7.19

calculations for Fe, Co, Ni, Cu, Mn, and FeCoNiCuMn 13-atom nanoclusters were carried out here. When compared to single atom nanoclusters, it was discovered that random FeCoNiCuMn HEA had substantially higher *d*-states near Fermi-level (Figure 7). The case of Ni and Co exhibits maximum electronic redistribution below the Fermi level, while the case of Fe and Mn exhibits more hybridized *d*-states, above Fermi level. Thus, it can be deduced that the hybridized *d*-states of Ni and Co

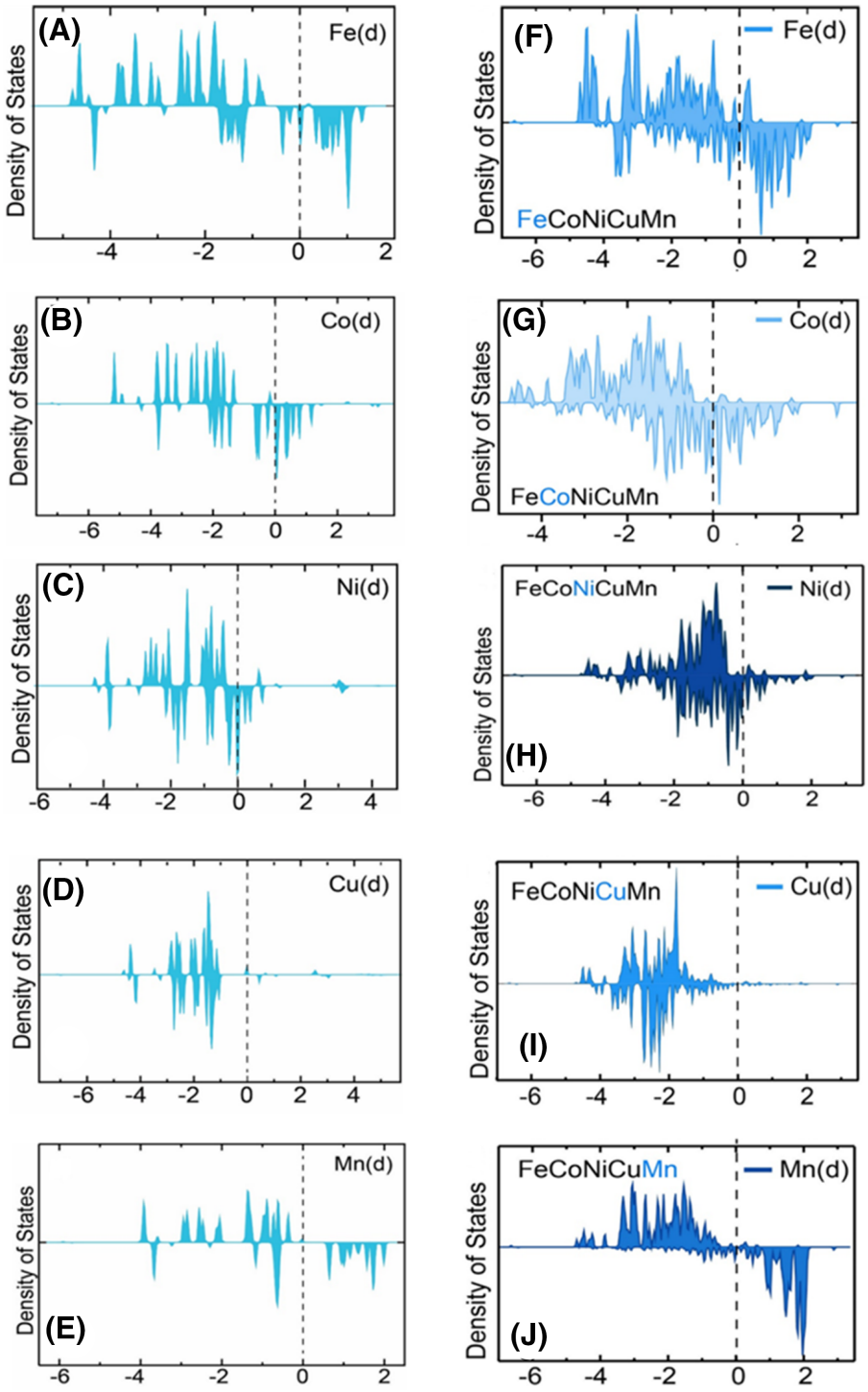

FIGURE 7 DOS of (A) Fe, (B) Ni, (C) Co, (D) Cu, and (E) Mn 13-atom nanocluster and DOS plots for d-states of (F) Co, (G) Fe, (H) Cu, (I) Mn, and (J) Ni in FeCoNiCuMn HEA.

contribute more to the HOMO (highest occupied molecular orbital) than the hybridized *d*-states of Fe and Mn contribute more to the LUMO (lowest unoccupied molecular orbitals).

4.3 | Post electrochemical studies

The post XPS analysis is carried out for FeCoNiCuMn HEA electrode, as shown in Figure S5A showing survey spectra. Starting with deconvoluted peak of Fe 2p (Figure S5B), the broad peaks are referred as Fe^{3+}, while other intense peaks are Fe^{0}, satellite shake up peaks. This change in intensity as well as peak position can be referred as transition between M^{n+} to M^{m+} during electrochemical redox reactions. Similarly for Co 2p (Figure S5C), the intense peaks are Co^{2+} of Co, while for Ni^{2+} (Figure S5D) shifts peak position slightly, while other less intensity peaks are Ni^{0} and satellite peaks, respectively. The Cu^{+} peaks of Cu 2p (Figure S5E) remains unaltered while intensity changes. The Mn 2p (Figure S5F) deconvoluted peaks are noted as Mn^{0}, Mn^{4+}, and Mn^{sat}, respectively. The broad rise of oxygen is due to strong interaction with electrolytic aqueous KOH electrolyte. The detailed spectrum analysis shows oxidation states remains unaltered even after 10000 cycles showing stability of FeCoNiCuMn HEA as promising supercapacitive electrode material.

We utilize the *d*-states to describe the DOS in individual nanoclusters as well as elements in high entropy system. As seen in Figure 7, the change in adsorption energy is greatest when Mn atoms are located in the FeCoNiCuMn nanocluster (Figure 7F-J) as opposed to individual nanoclusters Figure 7A-E. But out of all the elements, Ni was found to have the least difference in adsorption energy. The adsorption energies were calculated using the formulas:

$$\begin{aligned} &E(OH@Fe-Co-Ni-Cu-Mn) \\ &= E(*OH) - (E^{*} + (E(H_2O) - 0.5^{*} E(H_2))) \end{aligned} \quad (5)$$

where *E* (OH@ Fe-Co-Ni-Cu-Mn) is the adsorption energies of *OH on different sites of Fe-Co-Ni-Cu-Mn, * represents pristine nanocluster, and OH with * superscript denotes the species being adsorbed on the nanocluster, $E(H_2O)$ is the energy of water molecule and $E(H_2)$ is the energy of hydrogen molecule. Figure S3f shows difference in adsorption of OH^{-} of each individual element.

As shown in the Figure 8A, the '*b*' value of FeCoNiCuMn is around 0.67 at 0.2 V while for FeCoNiCuZn it is around 0.6 at 0.4 V. For Mn replacing Zn in the FeCoNiCuX high entropy system results in more pseudocapacitive dominance, which was observed from power law. With multiple Mn states, it is additionally more reactive towards oxygen which results in Mn-oxides which are pseudocapacitive in nature. The same results are mimicked for percentage of diffusion and surface controlled contribution in total charge for various scan rates Figure 8B. For FeCoNiCuMn there was a little dominance of surface controlled process to the total charge as compared to FeCoNiCuZn. In addition, the density function theory comparison with FeCoNiCuMn/Zn also displayed in Figure 8C,D. In order to investigate the variation in the adsorption energy for OH species, OH was adsorbed on every single 13-atom nanocluster, and the adsorption energy of each FeCoNiCuZn HEA element was computed (Figure 8E) using the following formula.[59]

As described by Hammer and Norskov,[105] the first moment of *d*-DOS (density of states for *d*-electrons of metal) is the *d*-band center.

$$\varepsilon_d = \frac{\int_{-\infty}^{\infty} n_d(\varepsilon)\varepsilon d\varepsilon}{\int_{-\infty}^{\infty} n_d(\varepsilon) d\varepsilon} \quad (6)$$

The metal *d*-band hybridizes with adsorbate bonding orbitals to form bonding and anti-bonding orbitals. Since the renormalized bonding orbitals of adsorbate is lower in energy, the bonding orbitals ($d-\sigma$) thus formed will be occupied by adsorbate electrons (Figure 8F). It is the filling of anti-bonding orbitals ($d-\sigma$)* that determines the strength of the metal-adsorbate bond. Smaller the difference between Fermi level and *d*-band center ($E_f - E_d$), more unoccupied antibonding orbitals are present above the Fermi level, thus leading to stronger bonding. The $E_f - E_d$ value of Mn is lesser than that of Zn (see Table 4). The *d*-states near the Fermi level has a direct influence on supercapacitance, as mentioned earlier. Hence, the replacement of Mn in place of Zn improves the supercapacitance of the HEA, due to availability of more *d*-states near the Fermi level. These results explain the replacement of Mn over Zn in HEA system providing more pseudocapacitive nature.

5 | CONCLUSION

In conclusion, the article demonstrates a strategy to synthesize nanostructured HEA comprising of FeCoNiCuMn by simple induction melting followed by ball milling. The prepared FeCoNiCuMn HEA electrode showed improved CV and good GCD response for three electrodes with

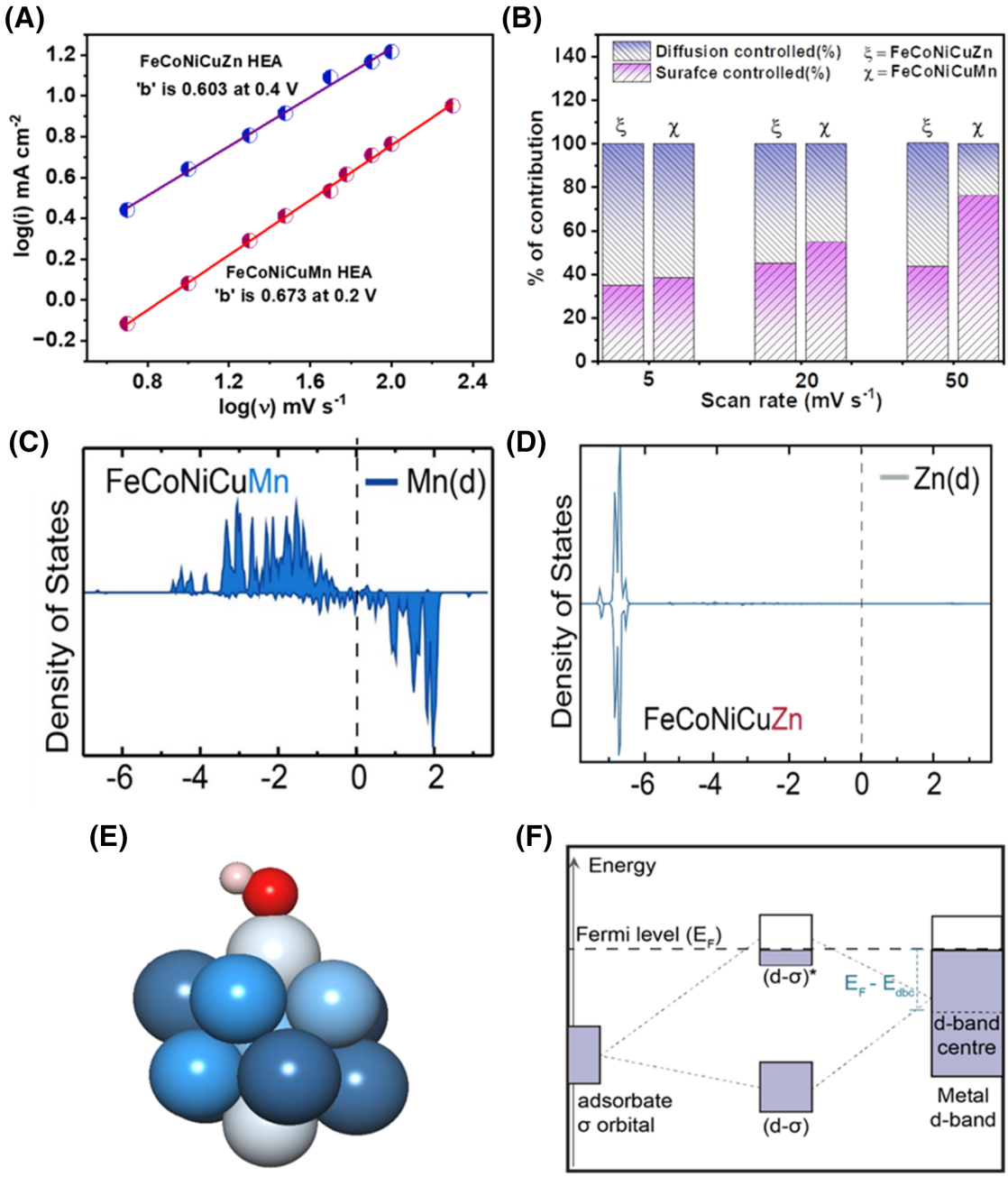

FIGURE 8 (A) Comparison of '*b*' value of FeCoNiCuMn and FeCoNiCuZn HEA electrode at 0.2 and 0.4 V, respectively, (B) Comparison of surface controlled and diffusion controlled percentages for both kinds of electrode, (C, D) d-band analysis for the Mn and Zn in the respective HEAs, (E) OH species adsorbed on Co atom of 13-atom FeCoNiCuMn HEA nanocluster. Nanocluster with different shades of blue represents FeCoNiCuMn HEA, red represents oxygen atom and off-white color represents hydrogen, and (F) d-band center.

maximum C_s of 192.5 at 2 A g^{-1} in both positive as well as negative voltage range. Green graphene (GG) is prepared from pyrolysis of rice straw (agricultural wastage) and used it as anode, which displays a highest C_s of 410 F g^{-1} at 2 A g^{-1} (560 F g^{-1} at 5 mVs^{-1}) in three electrode system. Due to their respective significant performance in both positive and negative potential window, fabrication of ASC device was considered with 3 M KOH electrolyte which was operated up to 1.7 V potential window. This wide voltage window device displays a Cs of 83.22 F g^{-1} at 2 A g^{-1} with a specific energy of 33.4 Wh kg^{-1} by consuming specific power of 1.7 kW kg^{-1}. We have thoroughly examined the *d*-band center for each elements associated with the FeCoNiCuMn HEA. We explain the replacement of Zn element with Mn in the high entropy system in terms of *d*-band center and its effects on improving pseudocapacitive nature in the system.

ACKNOWLEDGMENTS

C.S.T. acknowledges Core research grant of SERB-India, STARS project by MHRD-India, DAE Young Scientist Research Award (DAEYSRA), and AOARD (Asian Office of Aerospace Research and Development) grant no. FA2386-23-14034 and Naval research board (NRB) for their funding support.

CONFLICT OF INTEREST STATEMENT

The authors declare no conflicts of interest.

DATA AVAILABILITY STATEMENT

The data that support the findings of this study are available in Supporting Files online.

REFERENCES

1. Wang G, Zhang L, Zhang J. A review of electrode materials for electrochemical supercapacitors. *Chem Soc Rev*. 2012;41:797-828. doi:10.1039/C1CS15060J
2. Chen GZ. Supercapacitor and supercapattery as emerging electrochemical energy stores. *Int Mater Rev*. 2017;62:173-202. doi:10.1080/09506608.2016.1240914
3. An C, Zhang Y, Guo H, Wang Y. Metal oxide-based supercapacitors: progress and prospectives. *Nanoscale Adv*. 2019;1:4644-4658. doi:10.1039/C9NA00543A
4. Dahiya Y, Hariram M, Kumar M, Jain A, Sarkar D. Modified transition metal chalcogenides for high performance supercapacitors: current trends and emerging opportunities. *Coord Chem Rev*. 2022;451:214265. doi:10.1016/j.ccr.2021.214265
5. Hemanth NR, Kandasubramanian B. Recent advances in 2D MXenes for enhanced cation intercalation in energy harvesting applications: a review. *Chem Eng J*. 2020;392:123678. doi:10.1016/j.cej.2019.123678
6. Xu T, Wang Y, Xue Y, Li J, Wang Y. MXenes@metal-organic framework hybrids for energy storage and electrocatalytic application: insights into recent advances. *Chem Eng J*. 2023;470:144247. doi:10.1016/j.cej.2023.144247
7. Dong D, Xiao Y. Recent progress and challenges in coal-derived porous carbon for supercapacitor applications. *Chem Eng J*. 2023;470:144441. doi:10.1016/j.cej.2023.144441
8. Deng W, Liu W, Zhu H, Chen L, Liao H, Chen H. Click-chemistry and ionic cross-linking induced double cross-linking ionogel electrolyte for flexible lithium-ion batteries. *J. Energy Storage*. 2023;72:108509. doi:10.1016/j.est.2023.108509
9. Deng W, Xu Y, Zhang X, et al. (NH4)2Co2V10O28·16H2O/(NH4)2V10O25·8H2O heterostructure as cathode for high-performance aqueous Zn-ion batteries. *J Alloys Compd*. 2022;903:163824. doi:10.1016/j.jallcom.2022.163824
10. Zeng G, Wang Y, Lou X, Chen H, Jiang S, Zhou W. Vanadium oxide/carbonized chestnut needle composites as cathode materials for advanced aqueous zinc-ion batteries. *J. Energy Storage*. 2024;77:109859. doi:10.1016/j.est.2023.109859
11. Deng W-N, Li Y-H, Xu D-F, Zhou W, Xiang K-X, Chen H. Three-dimensional hierarchically porous nitrogen-doped carbon from water hyacinth as selenium host for high-performance lithium–selenium batteries. *Rare Met*. 2022;41:3432-3445. doi:10.1007/s12598-022-02022-0
12. Wen X, Luo J, Xiang K, Zhou W, Zhang C, Chen H. High-performance monoclinic WO3 nanospheres with the novel NH4+ diffusion behaviors for aqueous ammonium-ion batteries. *Chem Eng J*. 2023;458:141381. doi:10.1016/j.cej.2023.141381
13. Li L, Nam JS, Kim MS, et al. Sulfur–carbon electrode with PEO-LiFSI-PVDF composite coating for high-rate and long-life lithium–sulfur batteries. *Adv Energy Mater*. 2023;13:2302139. doi:10.1002/aenm.202302139
14. Liu Y, Xiang K, Zhou W, Deng W, Zhu H, Chen H. Investigations on tunnel-structure MnO 2 for utilization as a high-voltage and long-life cathode material in aqueous ammonium-ion and hybrid-ion batteries. *Small*. 2023;20:e2308741. doi:10.1002/smll.202308741
15. Guo Z, Han X, Zhang C, et al. Activation of biomass-derived porous carbon for supercapacitors: a review. *Chin Chem Lett*. 2023;35:109007. doi:10.1016/j.cclet.2023.109007
16. Yi Z, Chen Z, Yin K, Wang L, Wang K. Sensing as the key to the safety and sustainability of new energy storage devices. *Prot. Control Mod. Power Syst.* 2023;8:27. doi:10.1186/s41601-023-00300-2
17. Yu X, Shang Y, Zheng L, Wang K. Application of nanogenerators in the field of acoustics. *ACS Appl Electron Mater*. 2023;5:5240-5248. doi:10.1021/acsaelm.3c00996
18. Ma N, Yin H, Wang K. Prediction of the remaining useful life of supercapacitors at different temperatures based on improved long short-term memory. *Energies*. 2023;16:5240. doi:10.3390/en16145240
19. Liu Y, Wang L, Li D, Wang K. State-of-health estimation of lithium-ion batteries based on electrochemical impedance spectroscopy: a review. *Prot Control Mod Power Syst*. 2023;8:41. doi:10.1186/s41601-023-00314-w
20. Hussain I, Lamiel C, Ahmad M, et al. High entropy alloys as electrode material for supercapacitors: a review. *J Energy Storage*. 2021;44:103405. doi:10.1016/j.est.2021.103405
21. Wang Y, Wang Y. High-entropy alloys in catalyses and supercapacitors: Progress, prospects. *Nano Energy*. 2022;104:107958. doi:10.1016/j.nanoen.2022.107958
22. Amiri A, Shahbazian-Yassar R. Recent progress of high-entropy materials for energy storage and conversion. *J Mater Chem A*. 2021;9:782-823. doi:10.1039/D0TA09578H
23. Yin Y, Zhang W-B, Zhang X-L, et al. Low dimensional high entropy oxide (FeCoCrMnNi)3O4 for supercapacitor application. *Dalt Trans*. 2023;52:9005-9016. doi:10.1039/D3DT00909B
24. Talluri B, Aparna ML, Sreenivasulu N, Bhattacharya SS, Thomas T. High entropy spinel metal oxide (CoCrFeMnNi)3O4 nanoparticles as a high-performance supercapacitor electrode material. *J. Energy Storage*. 2021;42:103004. doi:10.1016/j.est.2021.103004
25. Liang B, Ai Y, Wang Y, Liu C, Ouyang S, Liu M. Spinel-type (FeCoCrMnZn)3O4 high-entropy oxide: facile preparation and supercapacitor performance. *Materials (Basel)*. 2020;13:5798. doi:10.3390/ma13245798
26. Kong K, Hyun J, Kim Y, Kim W, Kim D. Nanoporous structure synthesized by selective phase dissolution of AlCoCrFeNi high entropy alloy and its electrochemical properties as supercapacitor electrode. *J Power Sources*. 2019;437:226927. doi:10.1016/j.jpowsour.2019.226927
27. Xu X, Du Y, Wang C, et al. High-entropy alloy nanoparticles on aligned electronspun carbon nanofibers for

supercapacitors. *J Alloys Compd*. 2020;822:153642. doi:10.1016/j.jallcom.2020.153642

28. Lal MS, Sundara R. High entropy oxides: a cost-effective catalyst for the growth of high yield carbon nanotubes and their energy applications. *ACS Appl Mater Interfaces*. 2019;11:30846-30857. doi:10.1021/acsami.9b08794
29. Lal MS, Sundara R. Multifunctional high entropy oxides incorporated functionalized biowaste derived activated carbon for electrochemical energy storage and desalination. *Electrochim Acta*. 2022;405:139828. doi:10.1016/j.electacta.2021.139828
30. Verma A, Kim KH, Mathur S, Lee D. Interdependence of the electrical performance of NiCuFeCoMn multi-structure carbonates as electrode material for supercapacitors. *J Alloys Compd*. 2022;922:166222. doi:10.1016/j.jallcom.2022.166222
31. Katkar PK, Marje SJ, Parale VG, et al. Fabrication of a high-performance hybrid supercapacitor based on hydrothermally synthesized highly stable cobalt manganese phosphate thin films. *Langmuir*. 2021;37:5260-5274. doi:10.1021/acs.langmuir.1c00243
32. Katkar PK, Padalkar NS, Patil AM, et al. Development of amorphous Fe-doped nickel-cobalt phosphate (Fe_x NiCo $[PO_4]_2$) nanostructure for enhanced performance of solid-state asymmetric supercapacitors. *Int J Energy Res*. 2022;46:12039-12056. doi:10.1002/er.7969
33. Katkar PK, Kadam AN, Jerng S-K, Chun S-H, Lee S-W. Rational design of redox active amorphous Ni-Mn phosphate anchored on vertical graphene nanohills (VGNHs) for solid-state energy storage device. *J Alloys Compd*. 2023;968:171935. doi:10.1016/j.jallcom.2023.171935
34. Verma A, Singh H, Mahton Y, Saha P, Tiwary CS, Bhattacharya J. Use of waste to wealth process derived sustainable silica-rich graphene analogues to provide enhanced corrosion resistance properties for coatings on carbon steel, exposed to marine environments. *Surf Coatings Technol*. 2023;464:129420. doi:10.1016/j.surfcoat.2023.129420
35. Xiang W, Zhang X, Chen J, et al. Biochar technology in wastewater treatment: a critical review. *Chemosphere*. 2020;252:126539. doi:10.1016/j.chemosphere.2020.126539
36. Abioye AM, Ani FN. Recent development in the production of activated carbon electrodes from agricultural waste biomass for supercapacitors: a review. *Renew Sustain Energy Rev*. 2015;52:1282-1293. doi:10.1016/j.rser.2015.07.129
37. Athanasiou M, Yannopoulos SN, Ioannides T. Biomass-derived graphene-like materials as active electrodes for supercapacitor applications: a critical review. *Chem Eng J*. 2022;446:137191. doi:10.1016/j.cej.2022.137191
38. Wang J, Wang S. Preparation, modification and environmental application of biochar: a review. *J Clean Prod*. 2019;227:1002-1022. doi:10.1016/j.jclepro.2019.04.282
39. Choi W-M, Jo YH, Sohn SS, Lee S, Lee B-J. Understanding the physical metallurgy of the CoCrFeMnNi high-entropy alloy: an atomistic simulation study. *NPJ Comput Mater*. 2018;4:1. doi:10.1038/s41524-017-0060-9
40. Shim SH, Pouraliakbar H, Hong SI. High strength dual fcc phase CoCuFeMnNi high-entropy alloy wires with dislocation wall boundaries stabilized by phase boundaries. *Mater Sci Eng A*. 2021;825:141875. doi:10.1016/j.msea.2021.141875
41. Karimi MA, Shamanian M, Enayati MH, Adamzadeh M, Imani M. Fabrication of a novel magnetic high entropy alloy with desirable mechanical properties by mechanical alloying and spark plasma sintering. *J Manuf Process*. 2022;84:859-870. doi:10.1016/j.jmapro.2022.10.048
42. Zhang L, Zhou M, Shao L, Wang W, Fan K, Qin Q. Reactions of Fe with H_2O and FeO with H_2. A combined matrix isolation FTIR and theoretical study. *J Phys Chem A*. 2001;105:6998-7003. doi:10.1021/jp010914n
43. Singh S, Pavithra N, Naik TSSK, et al. Removal of Pb ions using green Co_3O_4 nanoparticles: simulation, modeling, adsorption, and biological studies. *Environ Res*. 2023;222:115335. doi:10.1016/j.envres.2023.115335
44. Miao L-Z, Guo Y-X, Liu Z-Y, Li Y, Zhu J, Wu L. High-entropy alloy nanoparticles/biochar as an efficient catalyst for high-performance treatment of organic pollutants. *Chem Eng J*. 2023;467:143451. doi:10.1016/j.cej.2023.143451
45. Das S, Sanjay M, Singh Gautam AR, Behera R, Tiwary CS, Chowdhury S. Low bandgap high entropy alloy for visible light-assisted photocatalytic degradation of pharmaceutically active compounds: performance assessment and mechanistic insights. *J Environ Manage*. 2023;342:118081. doi:10.1016/j.jenvman.2023.118081
46. Huang K, Peng D, Yao Z, et al. Cathodic plasma driven self-assembly of HEAs dendrites by pure single FCC FeCoNiMnCu nanoparticles as high efficient electrocatalysts for OER. *Chem Eng J*. 2021;425:131533. doi:10.1016/j.cej.2021.131533
47. Sharma SK, Sharma G, Sharma A, et al. Synthesis of silica and carbon-based nanomaterials from rice husk ash by ambient fiery and furnace sweltering using a chemical method. *Appl Surf Sci Adv*. 2022;8:100225. doi:10.1016/j.apsadv.2022.100225
48. Araichimani P, Prabu KM, Kumar GS, et al. Rice husk-derived mesoporous silica nanostructure for supercapacitors application: a possible approach for recycling bio-waste into a value-added product. *Silicon*. 2022;14:10129-10135. doi:10.1007/s12633-022-01699-3
49. Gu J, Zhang H, He X, et al. Monolithic carbon nanosheets with rich pores for high-capacitance supercapacitor. *J Porous Mater*. 2020;27:487-494. doi:10.1007/s10934-019-00831-w
50. Haeri SZ, Ramezanzadeh B, Asghari M. A novel fabrication of a high performance SiO2-graphene oxide (GO) nanohybrids: characterization of thermal properties of epoxy nanocomposites filled with SiO2-GO nanohybrids. *J Colloid Interface Sci*. 2017;493:111-122. doi:10.1016/j.jcis.2017.01.016
51. Narayanan DP, Sankaran S, Narayanan BN. Novel rice husk ash: reduced graphene oxide nanocomposite catalysts for solvent free Biginelli reaction with a statistical approach for the optimization of reaction parameters. *Mater Chem Phys*. 2019;222:63-74. doi:10.1016/j.matchemphys.2018.09.078
52. Husain Z, Shakeelur Raheman AR, Ansari KB, et al. Nano-sized mesoporous biochar derived from biomass pyrolysis as electrochemical energy storage supercapacitor. *Mater Sci Energy Technol*. 2022;5:99-109. doi:10.1016/j.mset.2021.12.003
53. Ma Z-W, Liu H-Q, Lü Q-F. Porous biochar derived from tea saponin for supercapacitor electrode: effect of preparation technique. *J. Energy Storage*. 2021;40:102773. doi:10.1016/j.est.2021.102773
54. Chen C, Xu G, Wei X, Yang L. A macroscopic three-dimensional tetrapod-separated graphene-like oxygenated N-doped carbon nanosheet architecture for use in supercapacitors. *J Mater Chem A*. 2016;4:9900-9909. doi:10.1039/C6TA04062D

55. Wang J, Chen T, Xu B, Chen Y. Fabrication and characterization of porous Core–Shell graphene/SiO2 nanocomposites for the removal of cationic neutral red dye. *Appl Sci*. 2020;10:8529. doi:10.3390/app10238529
56. Simon P, Gogotsi Y, Dunn B. Where do batteries end and supercapacitors begin? *Science (80–)*. 2014;343:1210-1211. doi:10.1126/science.1249625
57. Noori A, El-Kady MF, Rahmanifar MS, Kaner RB, Mousavi MF. Towards establishing standard performance metrics for batteries, supercapacitors and beyond. *Chem Soc Rev*. 2019;48:1272-1341. doi:10.1039/c8cs00581h
58. Augustyn V, Simon P, Dunn B. Pseudocapacitive oxide materials for high-rate electrochemical energy storage. *Energ Environ Sci*. 2014;7:1597. doi:10.1039/c3ee44164d
59. Mohanty GC, Chowde Gowda C, Gakhad P, et al. Iron-cobalt-nickel-copper-zinc (FeCoNiCuZn) high entropy alloy as positive electrode for high specific capacitance supercapacitor. *Electrochim Acta*. 2023;470:143272. doi:10.1016/j.electacta.2023.143272
60. Mohanty GC, Gowda CC, Gakhad P, et al. High energy density liquid state asymmetric supercapacitor devices using Co-Cr-Ni-Fe-Mn high entropy alloy. *Mater. Adv*. 2023;4:3839-3852. doi:10.1039/d3ma00327b
61. Shen E, Song X, Chen Q, Zheng M, Bian J, Liu H. Spontaneously forming oxide layer of high entropy alloy nanoparticles deposited on porous carbons for supercapacitors. *ChemElectroChem*. 2021;8:260-269. doi:10.1002/celc.202001289
62. Jin T, Sang X, Unocic RR, et al. Mechanochemical-assisted synthesis of high-entropy metal nitride via a soft urea strategy. *Adv Mater*. 2018;30:1707512. doi:10.1002/adma.201707512
63. Sure J, Sri Maha Vishnu D, Kim H, Schwandt C. Facile electrochemical synthesis of nanoscale (TiNbTaZrHf)C high-entropy carbide powder. *Angew Chemie Int Ed*. 2020;59:11830-11835. doi:10.1002/anie.202003530
64. Yang Y, Chen B, Chen J, Hu L, Hu M. Preparation of (VNbTaZrHf)C high-entropy carbide nanoparticles via electro-deoxidation in molten salt and their supercapacitive behaviour. *Can Metall Quart*. 2022;61:389-397. doi:10.1080/00084433.2022.2058151
65. Tang P, Cao Y, Hao l, Lu M, Qiu W. The preparation of high-performance aqueous supercapacitor with high-entropy pyrochlore-type electrode and super-concentrated electrolyte. *Ceram Int*. 2022;48:2660-2669. doi:10.1016/j.ceramint.2021.10.050
66. Nan H, Lv S, Xu Z, et al. Inducing the cocktail effect in yolk-shell high-entropy perovskite oxides using an electronic structural design for improved electrochemical applications. *Chem Eng J*. 2023;452:139501. doi:10.1016/j.cej.2022.139501
67. Jiang W, Wang T, Chen H, et al. Room temperature synthesis of high-entropy Prussian blue analogues. *Nano Energy*. 2021;79:105464. doi:10.1016/j.nanoen.2020.105464
68. Jin H, Hu J, Wu S, et al. Three-dimensional interconnected porous graphitic carbon derived from rice straw for high performance supercapacitors. *J Power Sources*. 2018;384:270-277. doi:10.1016/j.jpowsour.2018.02.089
69. Zhu L, Shen F, Smith RL, Yan L, Li L, Qi X. Black liquor-derived porous carbons from rice straw for high-performance supercapacitors. *Chem Eng J*. 2017;316:770-777. doi:10.1016/j.cej.2017.02.034
70. Xu Z, Zhang X, Liang Y, et al. Green synthesis of nitrogen-doped porous carbon derived from rice straw for high-performance supercapacitor application. *Energy Fuel*. 2020;34:8966-8976. doi:10.1021/acs.energyfuels.0c01346
71. Nguyen NT, Le PA, Phung VBT. Biomass-derived carbon hooks on Ni foam with free binder for high performance supercapacitor electrode. *Chem Eng Sci*. 2021;229:116053. doi:10.1016/j.ces.2020.116053
72. Xu X, Sielicki K, Min J, et al. One-step converting biowaste wolfberry fruits into hierarchical porous carbon and its application for high-performance supercapacitors. *Renew Energy*. 2022;185:187-195. doi:10.1016/j.renene.2021.12.040
73. Zhang D, Sun L, Liu Q, et al. Ultra-high specific surface area porous carbon derived from chestnut for high-performance supercapacitor. *Biomass Bioenergy*. 2021;153:106227. doi:10.1016/j.biombioe.2021.106227
74. Yue X, Yang H, Cao Y, et al. Nitrogen-doped cornstalk-based biomass porous carbon with uniform hierarchical pores for high-performance symmetric supercapacitors. *J Mater Sci*. 2022;57:3645-3661. doi:10.1007/s10853-022-06891-9
75. Chen W, Wang X, Liu C, Luo M, Yang P, Zhou X. Rapid single-step synthesis of porous carbon from an agricultural waste for energy storage application. *Waste Manag*. 2020;102:330-339. doi:10.1016/j.wasman.2019.10.058
76. Thirumal V, Yuvakkumar R, Ravi G, et al. Characterization of activated biomass carbon from tea leaf for supercapacitor applications. *Chemosphere*. 2022;291:132931. doi:10.1016/j.chemosphere.2021.132931
77. Zhang J, Chen H, Ma Z, et al. A lignin dissolution-precipitation strategy for porous biomass carbon materials derived from cherry stones with excellent capacitance. *J Alloys Compd*. 2020;832:155029. doi:10.1016/j.jallcom.2020.155029
78. Xu M, Huang Q, Lu J, Niu J. Green synthesis of high-performance supercapacitor electrode materials from agricultural corncob waste by mild potassium hydroxide soaking and a one-step carbonization. *Ind Crops Prod*. 2021;161:113215. doi:10.1016/j.indcrop.2020.113215
79. Baig MM, Gul IH. Conversion of wheat husk to high surface area activated carbon for energy storage in high-performance supercapacitors. *Biomass Bioenergy*. 2021;144:105909. doi:10.1016/j.biombioe.2020.105909
80. Charoensook K, Huang C-L, Tai H-C, et al. Preparation of porous nitrogen-doped activated carbon derived from rice straw for high-performance supercapacitor application. *J Taiwan Inst Chem Eng*. 2021;120:246-256. doi:10.1016/j.jtice.2021.02.021
81. Li S, Chen Q, Gong Y, et al. "One-step" carbonization activation of garlic seeds for honeycomb-like hierarchical porous carbon and its high supercapacitor properties. *ACS Omega*. 2020;5:29913-29921. doi:10.1021/acsomega.0c04190
82. Phiri J, Dou J, Vuorinen T, Gane PAC, Maloney TC. Highly porous willow wood-derived activated carbon for high-performance supercapacitor electrodes. *ACS Omega*. 2019;4:18108-18117. doi:10.1021/acsomega.9b01977
83. Yu P, Liang Y, Dong H, et al. Rational synthesis of highly porous carbon from waste bagasse for advanced supercapacitor application. *ACS Sustain. Chem. Eng.* 2018;6:15325-15332. doi:10.1021/acssuschemeng.8b03763

84. Chen X, Chi M, Xing L, et al. Natural plant template-derived cellular framework porous carbon as a high-rate and long-life electrode material for energy storage. *ACS Sustain. Chem. Eng.* 2019;7:5845-5855. doi:10.1021/acssuschemeng.8b05777
85. Guan L, Pan L, Peng T, et al. Synthesis of biomass-derived nitrogen-doped porous carbon nanosheests for high-performance supercapacitors. *ACS Sustain. Chem. Eng.* 2019;7:8405-8412. doi:10.1021/acssuschemeng.9b00050
86. Peng L, Liang Y, Huang J, et al. Mixed-biomass wastes derived hierarchically porous carbons for high-performance electrochemical energy storage. *ACS Sustain Chem Eng*. 2019;7:10393-10402. doi:10.1021/acssuschemeng.9b00477
87. Chen F, Ji Y, Deng Y, Ren F, Tan S, Wang Z. Ultrasonic-assisted fabrication of porous carbon materials derived from agricultural waste for solid-state supercapacitors. *J Mater Sci*. 2020;55:11512-11523. doi:10.1007/s10853-020-04751-y
88. Lukatskaya MR, Dunn B, Gogotsi Y. Multidimensional materials and device architectures for future hybrid energy storage. *Nat Commun*. 2016;7:1-13. doi:10.1038/ncomms12647
89. Hussain I, Hussain T, Yang S, et al. Integration of CuO nanosheets to Zn-Ni-Co oxide nanowire arrays for energy storage applications. *Chem Eng J*. 2021;413:127570. doi:10.1016/j.cej.2020.127570
90. Hussain I, Lee JM, Iqbal S, et al. Preserved crystal phase and morphology: electrochemical influence of copper and iron co-doped cobalt oxide and its supercapacitor applications. *Electrochim Acta*. 2020;340:135953. doi:10.1016/j.electacta.2020.135953
91. Agarwal A, Majumder S, Sankapal BR. Ni3P2O8 nanodots anchored multiwalled carbon nanotubes composite for flexible all-solid-state symmetric supercapacitor. *J. Energy Storage*. 2023;58:106396. doi:10.1016/j.est.2022.106396
92. Veerapandi G, Prabhu S, Ramesh R, Govindan R, Sekar C. Pseudo spin-ladder CaCu2O3 nanostructures as potential electrode material for asymmetric supercapacitors. *J. Energy Storage*. 2022;48:104051. doi:10.1016/j.est.2022.104051
93. Al Ojeery A, ul Hassan H, Al Balawi SA, Iqbal MW, Afzal AM, Hadia NMA. Growth of AgCoS@CNTs composite on nickel foam to enrich the redox active sites for battery-supercapacitor hybrid energy storage device. *J Phys Chem Solid*. 2023;180:111473. doi:10.1016/j.jpcs.2023.111473
94. Xu Y, Hou S, Yang G, Wang X, Lu T, Pan L. Synthesis of bimetallic NixCo1-xP hollow nanocages from metal-organic frameworks for high performance hybrid supercapacitors. *Electrochim Acta*. 2018;285:192-201. doi:10.1016/j.electacta.2018.07.211
95. Mirghni AA, Madito MJ, Masikhwa TM, Oyedotun KO, Bello A, Manyala N. Hydrothermal synthesis of manganese phosphate/graphene foam composite for electrochemical supercapacitor applications. *J Colloid Interface Sci*. 2017;494:325-337. doi:10.1016/j.jcis.2017.01.098
96. Wu C, Cai J, Zhang Q, et al. Hierarchical mesoporous zinc–nickel–cobalt ternary oxide nanowire arrays on nickel foam as high-performance electrodes for supercapacitors. *ACS Appl Mater Interfaces*. 2015;7:26512-26521. doi:10.1021/acsami.5b07607
97. Lei X, Ge S, Tan Y, et al. High capacity and energy density of Zn–Ni–Co–P nanowire arrays as an advanced electrode for aqueous asymmetric supercapacitor. *ACS Appl Mater Interfaces*. 2020;12:9158-9168. doi:10.1021/acsami.9b17038
98. Li B, Gu P, Feng Y, et al. Ultrathin nickel-cobalt phosphate 2D nanosheets for electrochemical energy storage under aqueous/solid-state electrolyte. *Adv Funct Mater*. 2017;27:1605784. doi:10.1002/adfm.201605784
99. Xu K, Li W, Liu Q, et al. Hierarchical mesoporous NiCo2O4@MnO2 core–shell nanowire arrays on nickel foam for aqueous asymmetric supercapacitors. *J Mater Chem A*. 2014;2:4795. doi:10.1039/c3ta14647b
100. Zhang Z, Zhang H, Zhang X, et al. Facile synthesis of hierarchical CoMoO 4 @NiMoO 4 core–shell nanosheet arrays on nickel foam as an advanced electrode for asymmetric supercapacitors. *J Mater Chem A*. 2016;4:18578-18584. doi:10.1039/C6TA06848K
101. Jangu S, Satpathy BK, Raju M, Jacob C, Pradhan D. Synthesis of V-shaped MnO 2 nanostructure and its composites with reduced graphene oxide for supercapacitor application. *Dalt. Trans.* 2021;50:6878-6888. doi:10.1039/D1DT00422K
102. Sha W, Guo Y, Yuan Q, et al. Artificial intelligence to power the future of materials science and engineering. *Adv Intell Syst*. 2020;2:1900143. doi:10.1002/aisy.201900143
103. Nørskov JK, Studt F, Abild-Pedersen F, Bligaard T. *Fundamental Concepts in Heterogeneous Catalysis*. Hoboken, NJ, USA: John Wiley & Sons, Inc; 2014. doi:10.1002/9781118892114
104. Guan Y, Cong Y, Zhao R, et al. Regulating d-band Center of Ti 2 C MXene via Nb alloying for stable and high-efficient Supercapacitive performances. *Small*. 2023;19:e2301276. doi:10.1002/smll.202301276
105. Hammer B, Nørskov JK. Theoretical surface science and catalysis: calculations and concepts. *Adv Catal*. 2000;45:71-129. doi:10.1016/S0360-0564(02)45013-4

SUPPORTING INFORMATION

Additional supporting information can be found online in the Supporting Information section at the end of this article.

How to cite this article: Mohanty GC, Chowde Gowda C, Gakhad P, et al. Enhanced energy density of high entropy alloy (Fe-Co-Ni-Cu-Mn) and green graphene hybrid supercapacitor. *Energy Storage*. 2024;6(4):e668. doi:10.1002/est2.668